JGR Solid Earth

RESEARCH ARTICLE
10.1029/2024JB029900

Deep-Focus Earthquakes in Warm Slabs: Seismic Source Parameters in the Peru-Brazil Region

G. S. Leite Neto[1], **G. A. Prieto**[2], **and J. Julià**[1,3]

[1]Programa de Pós-Graduação em Geodinâmica e Geofísica, Universidade Federal do Rio Grande do Norte, Natal, Brazil, [2]Departamento de Geociencias, Universidad Nacional de Colombia, Bogotá, Colombia, [3]Departamento de Geofísica, Universidade Federal do Rio Grande do Norte, Natal, Brazil

Key Points:

- Seismic source parameters were determined for 13 deep-focus earthquakes in the Peru-Brazil region
- Significant variations in stress drop and radiation efficiency were found to occur within a narrow seismic zone in our study region
- We propose that melting may play a role in explaining the coexistence of dissipative and brittle-like ruptures in the Peru-Brazil region

Supporting Information:

Supporting Information may be found in the online version of this article.

Correspondence to:

G. S. Leite Neto,
leitenetogs@gmail.com

Citation:

Leite Neto, G. S., Prieto, G. A., & Julià, J. (2025). Deep-focus earthquakes in warm slabs: Seismic source parameters in the Peru-Brazil region. *Journal of Geophysical Research: Solid Earth*, *130*, e2024JB029900. https://doi.org/10.1029/2024JB029900

Received 10 JUL 2024
Accepted 5 FEB 2025

Author Contributions:

Conceptualization: G. S. Leite Neto
Data curation: G. S. Leite Neto
Formal analysis: G. S. Leite Neto
Investigation: G. S. Leite Neto
Methodology: G. S. Leite Neto, G. A. Prieto
Supervision: G. A. Prieto, J. Julià
Validation: G. A. Prieto, J. Julià
Visualization: G. S. Leite Neto
Writing – original draft: G. S. Leite Neto
Writing – review & editing: G. A. Prieto, J. Julià

Abstract Deep-focus earthquakes pose a significant challenge because their occurrence under extreme pressure and temperature conditions should inhibit nucleation through conventional brittle-failure. Transformational faulting is generally accepted as a most plausible mechanism to explain deep-focus seismicity, but it encounters limitations in warm slabs like Nazca because warm temperatures may hinder the preservation of a metastable olivine wedge. Aiming at elucidating the conditions and processes driving deep seismicity in warm slabs, we determined seismic source parameters (stress drop, seismic moment, radiated energy, seismic efficiency) for 13 deep-focus earthquakes ($4.8 \leq Mw \leq 7.4$) in the Peru-Brazil border region. Our results suggest that variations in stress drop can be significant (5–90 MPa) and that scaling between stress drop and seismic moment holds for a wider range of magnitudes (Mw 4.8 to 7.4) than previously reported. Radiated energies are in the 6.8×10^{10}–1.9×10^{16} J range, with earthquakes in the 6.4–7.4 Mw magnitude range displaying the largest values (4.2×10^{14}–1.9×10^{16} J). Most importantly, variable radiation efficiencies (0.1–1.4) suggest the coexistence of dissipative and brittle-like ruptures within the slab segment. We propose that these values reflect different degrees of melting involved in the rupture process, possibly controlled by the release of water from hydrous phases in the source region. Moreover, dehydration reactions would be triggered by either the latent heat released from phase transformations or by shear heating, establishing an interplay between thermal runaway enhanced by melting and phase transformations promoted by the release of water.

Plain Language Summary Deep-focus earthquakes are puzzling because they occur under extreme pressure and temperature conditions that should inhibit brittle-failure. Transformational faulting is often regarded as a likely mechanism, but it faces limitations in explaining ruptures in warm slabs like Nazca. Aiming at understanding conditions and processes driving deep seismicity in warm slabs, we assessed seismic source parameters for 13 deep-focus events with magnitudes from 4.8 to 7.4 Mw in the Peru-Brazil border region. We found significant variations in terms of both stress drop (5–90 MPa) and radiation efficiency (0.1–1.4) within the slab segment. We propose that variable efficiencies reflect different degrees of melting involved in the rupture process, possibly controlled by the release of water from hydrous phases in the source region. Dehydration reactions would be triggered by either the latent heat released from transformational faulting or by shear heating, establishing an interplay between thermal runaway enhanced by melting and phase transformations promoted by the release of water.

1. Introduction

Deep earthquakes are defined as those happening at depths of 70 km or larger, and their very occurrence has puzzled seismologists due to their nucleation under pressure and temperature conditions where brittle fracture is inhibited (Frohlich, 1989, 2006). Down to 300 km depth, it is believed that the release of water from hydrated minerals within the slab enables embrittlement through increased pore pressure, which reduces normal stress and cohesive strength within cracks (Raleigh, 1967) and/or pre-existing faults (Ranero et al., 2003); at depths larger than 300 km, however, the progressive dehydration of the slab's crust and the negative sign of the volumetric changes of the reactions makes this mechanism more unlikely (Houston, 2015; Zhan, 2020). At larger depths, the origin of deep-focus earthquakes is often attributed to transformational faulting, which results from the formation and self-organization of anticracks—microscopic lenses filled with fine-grained superplastic material formed by transformation of olivine into its high-pressure polymorphs wadsleyite and ringwoodite—into a shear instability (Green & Burnley, 1989; Green & Marone, 2002; Green & Zhou, 1996; Ohuchi et al., 2022). Most importantly, this mechanism requires the preservation of a metastable olivine wedge (MOW) within the core of a subducted

slab at mantle transition zone (MTZ) depths, where delayed phase transformations capable of triggering a shear instability would allow the nucleation of earthquakes at those great depths (Green & Zhou, 1996; Zhan, 2020).

The existence of a MOW strongly depends on the thermal state of the subducting plate (Green & Marone, 2002; Green & Zhou, 1996), which is often described by the thermal parameter ϕ calculated from the age and subduction speed of the oceanic lithosphere (Frohlich, 2006; Kirby et al., 1991, 1996). Warm plates such as Nazca ($\phi < 2{,}500$ km) (Frohlich, 2006), are not expected to host a MOW because their higher temperatures would favor olivine phase transformations close to nominal depths, thereby limiting the depth extent of the MOW within the MTZ. Numerical experiments show that only the coldest slabs (e.g., Tonga with $\phi > 10{,}000$ km) (Frohlich, 2006) would be able to sustain a MOW down to the base of the MTZ (Devaux et al., 1997; Mosenfelder et al., 2001), but, surprisingly, some warm slabs such as Nazca also exhibit deep-focus earthquakes at such depths (Frohlich, 2006). Recent studies have provided seismological evidence of a MOW in the Pacific slab under Japan (e.g., Furumura et al., 2016; Jiang & Zhao, 2011; Kawakatsu & Yoshioka, 2011; Shen & Zhan, 2020), which is characterized by a thermal parameter of $\phi \sim 5{,}000$–$7{,}000$ km (Frohlich, 2006). Although no such evidence has been reported for the Nazca slab, the existence of a MOW that nucleates deep-focus events has been assessed from analysis of focal plane solution and centroid depths (Leite Neto et al., 2024a).

The Brazilian Seismographic Network (RSBR) started operations in 2011 and slowly expanded operations within the Amazonian region after 2014 (Bianchi et al., 2018). RSBR broadband stations have provided an unprecedented coverage of deep-focus events with epicenters in the Peru-Brazil region, one of the two segments with regular deep-focus seismicity in South America (Figure 1) (Frohlich, 2006). Between 2014 and 2022, a total of 42 deep-focus earthquakes with magnitudes between 4.0 and 7.6 Mw and depths between 515 and 655 km occurred in this region, according to the USGS. A total of 25 events happened only in 2015, a year of anomalously intense seismic activity that included a well-studied 7.6 Mw doublet and several aftershocks (e.g., Jiménez et al., 2021; Ruiz et al., 2017; Ye et al., 2016; Zahradník et al., 2017). Indeed, most studies on deep-focus events, including those in South America, have usually focused on the largest ruptures (e.g., Estabrook, 1999; Kanamori et al., 1998; Zahradník et al., 2017), the smaller ones being mostly left unstudied. Moreover, a comparison of the parameters reported for larger earthquakes has often been difficult due to the variety of approaches utilized for retrieving them (e.g., Tibi et al., 2003). Therefore, the unprecedented additional coverage provided by RSBR, coupled with the occurrence of unusual seismic activity in 2015, represents a unique opportunity to investigate the physical mechanisms responsible for the nucleation of a broad range of deep-focus earthquakes in a warm slab.

In this work we study the seismic source parameters for these 42 deep-focus earthquakes, with the aim of investigating the physical mechanism behind their occurrence under South America. We were able to determine seismic moments, corner frequencies, stress drops, radiated energies and radiation efficiencies for a total of 13 events with magnitudes from 4.8 to 7.4 Mw. We show that variations in stress drop and radiation efficiency can be considerable within our study region, reflecting the coexistence of dissipative and brittle rupture. We argue that more dissipative ruptures are controlled by localized hydrated regions near the source, which can eventually dehydrate and induce melting within the fault zone. The occurrence of deep-focus events is then explained as the result of rupture initiation by transformational faulting followed by thermal runaway. The amount of melting during this last stage would be controlled by the amount of water that can be released through dehydration reactions (e.g., hydrous phase A), through either the latent heat released by the reaction or by shear heating near the fault zone. Moreover, we think that our interpretation reconciles the presence of water in the MTZ, as evidenced by sublithospheric diamonds, with the existence of a MOW responsible for the nucleation and observed depth-span of deep-focus earthquakes.

2. Data

Our data set comprises recordings from several broadband stations in South America (see details in Table S2 in Supporting Information S1), including those belonging to the international GSN (network codes II and IU) and GEOFON (GE) networks, as well as data from the national networks of Brazil (BR and NB), Colombia (CM), Ecuador (EC), and Chile (C and C1). It also included recordings from the temporary 3-Basin Project (XC) deployment, with stations installed in Uruguay, Argentina, Paraguay, Bolivia and Brazil, and the IPOC seismic network in Chile (CX) (Figure 1). Note that stations from the RSBR (black and gray triangles) were essential to provide upper-hemisphere coverage of the seismic focal sphere. Further details on the data set can be found in the Open Research section.

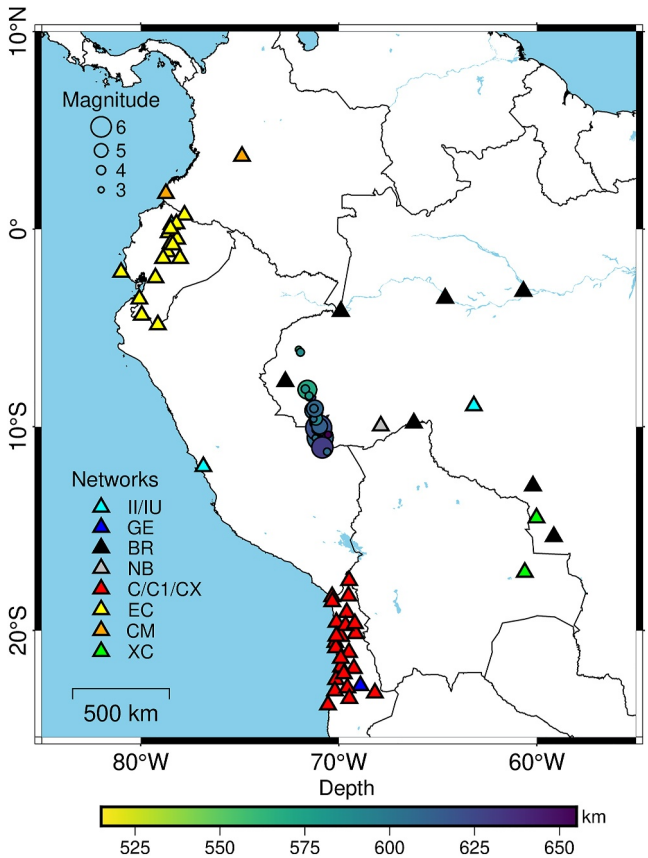

Figure 1. Distribution of the 55 seismic stations and 42 deep-focus earthquakes used in this study. Stations are colored by network. Black and gray stations belong to the RSBR subnetworks (NB and BR). Network codes follow the International Federation of Digital Seismograph Networks (FDSN) standards. A table with station information can be found in Table S2 in Supporting Information S1. Epicenters for the 2014–2022 deep-focus sequence are color-coded by depth and sized by magnitude, as reported in the USGS catalog (Table S1 in Supporting Information S1).

As mentioned above, our data set consisted of 42 deep-focus earthquakes with depths between 515 and 655 km and magnitudes between 4.0 and 7.6 Mw, as reported in the USGS catalog after 2014, coinciding with the deployment of RSBR stations in the Amazon region. As a pre-processing step, P- and S-wave arrival times were marked on the seismograms using the TauP algorithm (Crotwell et al., 1999) and based on the AK135 velocity model (Kennett et al., 1995). We used these times to cut the seismograms into windows starting 2 min before the P-wave arrival and lengths equal to one S-P interval after the S-wave arrival time, which resulted in seismograms longer than 360 s. This time window was found sufficient to encompass the entirety of P- and S-wave energy in the recordings. The instrument responses were then deconvolved from the corresponding seismograms, after removal of the mean and trend and the application of a 5% cosine taper. Next, displacement recordings were rotated into the great-circle-path to ensure the separation of P-SV and SH amplitudes into the rotated components (see examples in Figures S1 and S2 in Supporting Information S1).

3. Seismic Moments, Corner Frequencies, and Stress Drops

3.1. Determination of Source and Background Spectra

To calculate the spectra for each source-station pair we selected all local and regional stations at less than 1,500 km from the epicenter and cut the P- and S-wave segments from the corresponding seismograms using time windows of 40 and 100 s, respectively. These time windows were chosen to comprise the full body wave signal and were set with tolerances of 10% and 20% around the P- and S-wave arrival times, respectively. We retrieved P-wave windows from the vertical components only, while S-wave windows were obtained from all three components. The corresponding noise segments were obtained using the same window lengths, but stopping just right before the beginning of the P-wave window (e.g., Prieto et al., 2004). After the signal and noise segments were obtained, the mean and trend from each of these segments were removed before computing the spectra, which was obtained using the multitaper algorithm available in the open-source Multitaper python package (Prieto, 2022). This algorithm effectively minimizes the inherent limitations of non-parametric approaches (spectral leakage and high variance of the spectrum estimate) by applying multiple tapering and then averaging the resulting spectra employing an adaptive weighting (Thomson, 1982). We adopted a time-bandwidth product of 4 and a total of 6 tapers in all our estimations.

Based on the individual noise spectra computed for each source-station pair, an average background noise spectrum was developed for each station. These spectra are used to assess the signal-to-noise ratio (SNR) at a given station with respect to the individual P- and S-wave spectra for a given event. We chose to use average noise spectra for assessing SNR because individual noise spectra show a more moderate variability at a given station (see example in Figure S3 in Supporting Information S1). After analyzing station averages obtained from the arithmetic mean, the geometric mean, and the median of the individual noise spectra, we selected the geometric mean plus one standard deviation as the background noise spectrum for each station. Estimates from the arithmetic mean were found to be unsuitable due to their sensitivity to outliers; the median and the geometric mean provided similar results, so we chose the geometric mean plus one standard deviation to ensure a careful SNR evaluation (see Figure S3 in Supporting Information S1). Note that the method models individual source spectra, so average source spectra were not developed.

Finally, source and background noise spectra were resampled to display uniformly spaced values in the logarithmic scale (e.g., Abercrombie, 2015; Abercrombie et al., 2017; Ide et al., 2003). Note that, if spectra were left with uniformly spaced values in the linear scale, higher frequencies would be more densely sampled in the logarithmic scale and bias the source parameters estimates obtained from them. Additionally, the original number

of points for both P- and S-wave spectra was reduced from 4,000 to 10,000, respectively, to just 100, which were found enough for modeling purposes. To make sure that the spectra can be minimally modeled, only those with at least one decade in the log scale with points above the SNR threshold (SNR $\geq$ 3) were considered. Also, only events with spectra from at least 5 stations were considered for analysis, ensuring that events are minimally covered azimuthally.

3.2. Seismic Moments and Corner Frequencies

To determine the seismic moment (M_0) and corner frequency (f_c) for the events making up the seismic sequence, we employed the Cluster-Event Method (CEM) of Ko et al. (2012). This method considers clusters of nearby events to empirically constrain Q structure while ensuring stability of the inversion parameters by requiring that: (a) all spectra within a given cluster have the same Q for a given station; and (b) all spectra for a given event are described by the same values of M_0 and f_c. These constraints significantly reduce the number of parameters to be inverted for and increase the robustness of the inversion. In our implementation, considering the small number of relatively close events, we assumed a single cluster and constrained inverted parameters M_0, f_c (f_c^P and f_c^S), and Q (Q_P and Q_S) to be within reasonably tight ranges to speed up convergence. Thus, M_0 was forced to stay within $\pm$20% from the previous estimate from either the USGS catalog or the waveform inversion study of Leite Neto et al. (2024a), whichever was available (Table S1 in Supporting Information S1), f_c was allowed to vary in a broad range from 0.01 to 50 Hz, and Q was allowed to vary between 100 and 2000.

While conducting the CEM, we noted that Q_P and Q_S tended to reach the limit prescribed value (Q = 2,000) at most stations. This tendency was also observed after changing this maximum to values up to 5,000. To further investigate this, we checked how misfit behaves as function of Q_P and Q_S for event 8, as this is one of the largest ruptures in our sequence and produced the most data with sufficient high SNRs. As shown in Figure S4 in Supporting Information S1, a broad minimum is apparent across most of the stations, which prevents accurate determination of Q_P and Q_S. Because Q_P and Q_S are poorly constrained in most of our inversions, a systematic decrease in f_c estimates is introduced due to the trade-off between f_c and Q (e.g., Ko et al., 2012). To circumvent this issue, we simply fixed both Q_P and Q_S to 1,000 for every event-station pair and carry on with the inversion for M_0, f_c^P, and f_c^S. After considerable testing, we observed that this Q value, although large, satisfactorily models the fall-off of most of the P and S spectra (Figure 2). It is also consistent with the very high values found at MTZ depths beneath the Pacific (Booth et al., 2014) and agrees with estimates for the subducting Pacific plate in New Zealand (Eberhart-Phillips et al., 2008). Although we acknowledge that Q_P must be different from Q_S, we note that this difference becomes negligible for large Q values when modeling the spectrum fall-off.

The misfit function was defined as the L1-norm between observed and modeled spectra, and it was evaluated with respect to the Brune circular fault model (Brune, 1970; Havskov & Ottemoller, 2010). For each source-station pair, a general misfit was calculated as the sum of the individual misfits for the single P-wave spectrum, which was determined from the vertical seismogram, and up to three S-wave spectra, corresponding to the radial, transverse and vertical components. To prevent S-wave spectra from dominating the inversion, we adjusted the weight of the P spectrum based on the number of S spectra being utilized. Basically, before computing the general misfit for the source-station pair, the P-wave spectrum's misfit was multiplied by a number ranging from 1 to 3 depending on the number of S-wave spectra employed in the inversion. We solved for the global minimum using the Dual Annealing optimization algorithm implemented in the Scipy Optimization subpackage, which is a global optimization routine based on the combination of the Classic Simulated Annealing and the Fast Simulated Annealing (Tsallis, 1988; Tsallis & Stariolo, 1996; Xiang et al., 1997). After the classical simulated annealing process, this approach performs a local search around its solution, increasing the accuracy of the results. We configured this routine to perform a maximum of 100 iterations and use an initial temperature of 100,000, high enough to avoid entrapment by a local minimum. Uncertainties in M_0 and f_c were assessed through bootstrap resampling (Efron & Tibshirani, 1991). For each event, we constructed 100 ensembles, each comprising randomly selected samples from the original set of stations with replacement. The inversion was then performed for every ensemble, allowing us to produce confidence bounds for our estimates.

Using the approaches described above, we were able to determine M_0 and f_c for a total of 14 events (out of 42), as listed in Table 1. The remaining portion of the sequence did not meet our criteria for analysis due to either spectra with low SNR and/or fewer than five stations available for inversion. In general, the inverted parameters provided satisfactory fits to our observations, especially for the larger events (see Figure 2 and Figures S10–S23 in

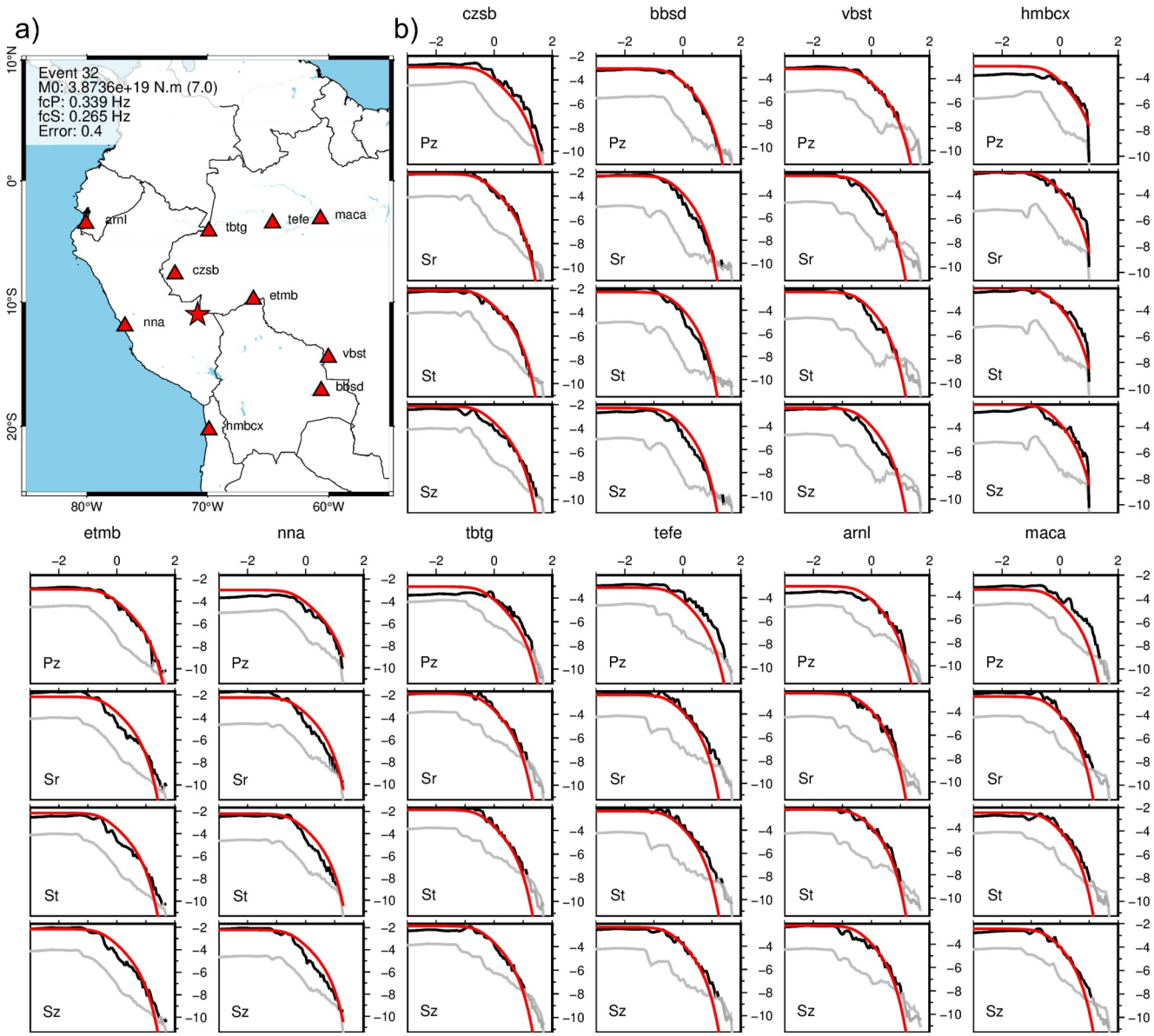

Figure 2. Selection of observed and predicted spectra for event 32 (7.0 Mw). On the map (a), the red star represents the epicenter, while red triangles indicate the stations selected for display in the figure (b). For each selected station, the black, red and light gray lines respectively represent the observed, modeled and background noise spectra. Segments of the observed spectra with low SNR are shown in dark gray and were not considered for inversion. The complete set of stations used in the inversion is displayed in Figure S17 in Supporting Information S1.

Supporting Information S1). Although the optimal fitting bandwidth can vary depending on the event and the station, it typically ranges from 0.05 to more than 10 Hz, although for the smaller events the lowest frequency can be of 0.5 Hz (Figure 3). We found f_c^P ranges from 0.16 to 3.7 Hz, f_c^S from 0.13 to 2.7 Hz, and M_0 from 2.08×10^{16} to 1.54×10^{20} N.m (Mw between 4.8 and 7.4). While M_0 was well constrained for all events, f_c tended to be less accurate for the smaller events (Mw < 6). More in particular, four events showed considerable uncertainties: event 22 (4.9 Mw), in both f_c^P and f_c^S estimates; event 35 (5.1 Mw), in the f_c^P estimate; and event 3 (5.4 Mw) and event 33 (4.8 Mw) in f_c^S (Figure 3). Therefore, we decided to disregard event 22 from our analysis but retain f_c^S for event 35 and f_c^P for events 3 and 33, thus proceeding with only 13 events.

Our results show that f_c^P decreases with M_0 as $M_0 \propto f_c^{-3.57}$ and f_c^S as $M_0 \propto f_c^{-4.19}$, different from the $M_0 \propto f_c^{-3}$ proportionality (e.g., Campus & Das, 2000), suggesting they are not self-similar (e.g., Prieto et al., 2004).

Table 1
Inverted Parameters for 14 Selected Events in the 2014–2022 Deep-Focus Sequence

Event	f_c^P (Hz)	f_c^S (Hz)	M_0 (N·m)	M_w	$\Delta\sigma^P$ (MPa)	$\Delta\sigma^S$ (MPa)	$\Delta\sigma$ (MPa)	E_R (J)	Ext%	η_R
3	0.851 ± 0.246	0.604 ± 4.921	$1.64 \times 10^{17} \pm 0.23 \times 10^{17}$	5.4	5.1 ± 0.84	–[a]	5.1 ± 0.84	5.80×10^{12}	67	1.58
8	0.163 ± 0.018	0.135 ± 0.011	$1.44 \times 10^{20} \pm 0.16 \times 10^{5}$	7.4	31.6 ± 0.04	56.0 ± 0.03	43.8 ± 0.04	1.06×10^{16}	43	0.38
9	0.174 ± 0.02	0.139 ± 0.010	$1.54 \times 10^{20} \pm 0.15 \times 10^{5}$	7.4	38.8 ± 0.06	61.8 ± 0.02	50.3 ± 0.04	1.23×10^{16}	32	0.37
19	0.252 ± 0.025	0.179 ± 0.013	$1.01 \times 10^{19} \pm 0.11 \times 10^{18}$	6.6	8.2 ± 0.10	9.1 ± 0.11	8.6 ± 0.10	1.49×10^{14}	22	0.39
22	1.87 ± 6.783	0.908 ± 6.878	$2.23 \times 10^{16} \pm 0.43 \times 10^{15}$	4.9	–[a]	–[a]	–	–	–	–
24	1.756 ± 0.583	0.756 ± 0.205	$4.30 \times 10^{16} \pm 0.13 \times 10^{16}$	5.1	11.1 ± 0.76	2.8 ± 0.14	6.9 ± 0.45	4.31×10^{11}	59	0.34
30	0.491 ± 0.041	0.288 ± 0.029	$3.70 \times 10^{18} \pm 0.51 \times 10^{3}$	6.3	20.9 ± 0.01	13.2 ± 0.01	17.0 ± 0.01	4.81×10^{13}	39	0.18
32	0.339 ± 0.044	0.265 ± 0.025	$3.87 \times 10^{19} \pm 0.82 \times 10^{4}$	7.0	72.1 ± 0.16	107.6 ± 0.09	89.8 ± 0.12	1.95×10^{16}	49	1.33
33	2.184 ± 0.301	2.757 ± 1.420	$2.08 \times 10^{16} \pm 0.86 \times 10^{15}$	4.8	11.0 ± 0.48	–[a]	11.0 ± 0.48	6.79×10^{10}	68	0.07
34	0.336 ± 0.049	0.276 ± 0.059	$1.33 \times 10^{19} \pm 0.20 \times 10^{4}$	6.7	25.5 ± 0.08	44.2 ± 0.43	34.8 ± 0.25	1.13×10^{15}	25	0.56
35	3.698 ± 11.315	1.167 ± 0.480	$5.61 \times 10^{16} \pm 0.59 \times 10^{16}$	5.1	–[a]	14.1 ± 2.46	14.1 ± 2.46	2.06×10^{12}	52	0.59
38	0.625 ± 0.101	0.442 ± 0.055	$7.30 \times 10^{17} \pm 0.31 \times 10^{16}$	5.9	9.0 ± 0.08	10.0 ± 0.06	9.5 ± 0.07	1.15×10^{13}	47	0.38
41	0.364 ± 0.037	0.276 ± 0.039	$4.88 \times 10^{18} \pm 0.15 \times 10^{18}$	6.4	11.9 ± 0.38	16.2 ± 0.55	14.1 ± 0.46	4.23×10^{14}	50	1.40
42	1.784 ± 0.475	1.022 ± 0.192	$6.07 \times 10^{16} \pm 0.42 \times 10^{16}$	5.2	17.4 ± 1.55	10.2 ± 0.78	13.8 ± 1.17	3.92×10^{11}	25	0.10

[a]High uncertainties in the corresponding f_c precluded the correct determination of the $\Delta\sigma$.

Departure from self-similarity was already recognized in previous works on intermediate-depth and deep-focus earthquakes, which suggested proportionality from $M_0 \propto f_c^{-3.12}$ to $M_0 \propto f_c^{-4.2}$ (e.g., Bos et al., 1998; Houston et al., 1998; Persh & Houston, 2004; Poli & Prieto, 2014; Tocheport et al., 2007).

3.3. Stress Drops

The static stress drop ($\Delta\sigma$) is an important parameter that quantifies the change in stress around the fault during its rupture (Lay & Wallace, 1995; Venkataraman & Kanamori, 2004). We determined $\Delta\sigma$ from M_0 and f_c estimates for each event after assuming a circular source as (Brune, 1970; Eshelby, 1957; Kaneko & Shearer, 2014; Madariaga, 1976):

$$\Delta\sigma = \frac{7}{16} M_0 \left(\frac{f_c}{k\beta}\right)^3 \quad (1)$$

in which f_c is the corner frequency, β is the S-wave velocity, and k is a constant that depends on wave type and the assumed theoretical model (Brune, 1970; Kaneko & Shearer, 2014; Madariaga, 1976). We used the model derived by Kaneko and Shearer (2014), which considers a circular rupture with a cohesive zone to avoid stress singularity at the rupture front (Madariaga, 1976). Based on our average f_c^P / f_c^S ratio (~1.41), we selected the model that considers a rupture velocity of $V_R = 0.9\beta$, for which $k = 0.38$ for P waves, and $k = 0.26$ for S waves. β was obtained from the AK135 velocity model based on event's depth (Kennett et al., 1995). Uncertainties in $\Delta\sigma$ were evaluated after propagating uncertainties in both M_0 and f_c through differentiation of Equation 1 (e.g., Prieto et al., 2007).

The $\Delta\sigma$ estimated from f_c^P range from 5.1 to 72.1 MPa, while estimates from f_c^S range from 2.8 to 107.6 MPa (Table 1). We determined the average $\Delta\sigma$ for each event based on the individual P and S corner frequency estimates, which resulted in variable values ranging between 5 and 90 MPa. Our confidence bounds are generally small, which reflects the accuracy of our f_c and M_0 estimates (Figure 4). It is worth noting that event 32 (Mw 7.0) shows the maximum $\Delta\sigma$ estimate, around 89.8 MPa. We also observed large $\Delta\sigma$ for the two biggest ruptures (Mw 7.4), corresponding to events 8 (43.8 MPa) and 9 (50.3 MPa), and event 34 (Mw 6.7, 34.8 MPa). The remaining events showed smaller values, $\Delta\sigma \leq 17$ MPa, with the smallest $\Delta\sigma$ found for event 3 (5.4 Mw, 5.1 MPa). Overall, there appears to be a trend of $\Delta\sigma$ increasing with M_0, albeit with considerable dispersion (Figure 4).

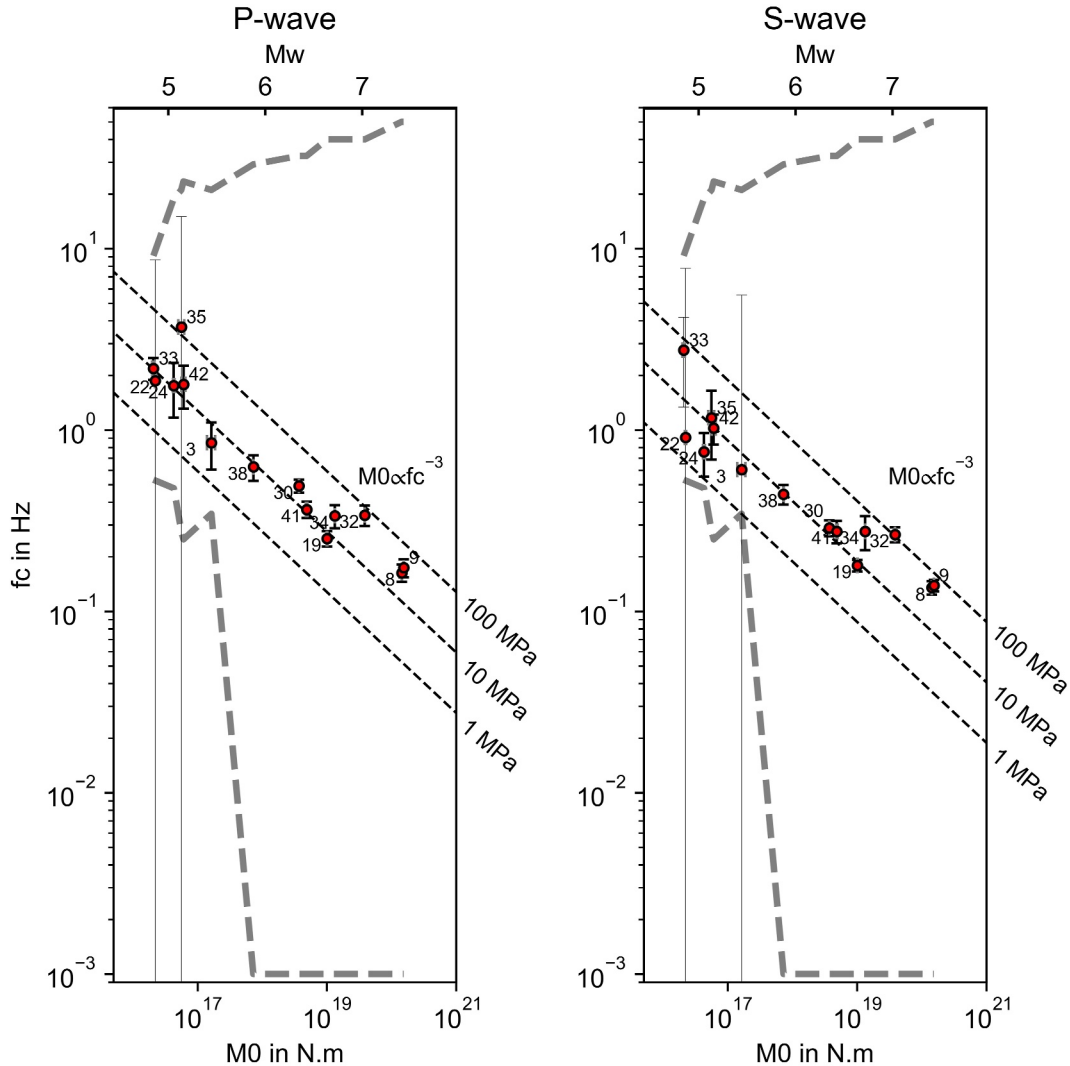

Figure 3. P- and S-wave corner frequencies as a function of seismic moment for the 14 events listed in Table 1. The uncertainties in f_c and M_0 are represented by vertical black bars and horizontal gray bars, respectively. Dashed black lines are for reference stress drops of 1, 10 and 100 MPa. Thick dashed gray lines delimit the frequency bandwidth of spectral fitting within which source parameters were determined for each event.

4. Radiated Energies, Scaled Energies, and Radiation Efficiencies

4.1. Radiated Energies From Body-Wave Spectra

The radiated energy (E_R) was determined for each event as the sum of the P- and S-wave radiation energies, E_R^P and E_R^S respectively (Boatwright & Fletcher, 1984; Mayeda & Walter, 1996; Prieto et al., 2004). We used the P-wave vertical displacement spectrum to determine E_R^P, and the vectorial sum of the radial, transverse, and vertical S-wave displacement spectra to determine E_R^S. All displacement spectra were corrected for attenuation and geometrical spreading and then transformed into moment rate spectra by differentiation (Havskov & Ottemoller, 2010). We then calculated an average spectrum for each phase based on all available spectra for a given event. In this step, only portions of the spectra with SNR ≥ 3 were considered. From the average moment-rate spectrum, $\omega M(\omega)$, we determined the energy in the frequency domain following (Baltay et al., 2010; Mayeda & Walter, 1996):

$$E_R^{P,S} = \frac{1}{4\pi^2 \rho c^5} \int_0^\infty |\omega M(\omega)|^2 d\omega \quad (2)$$

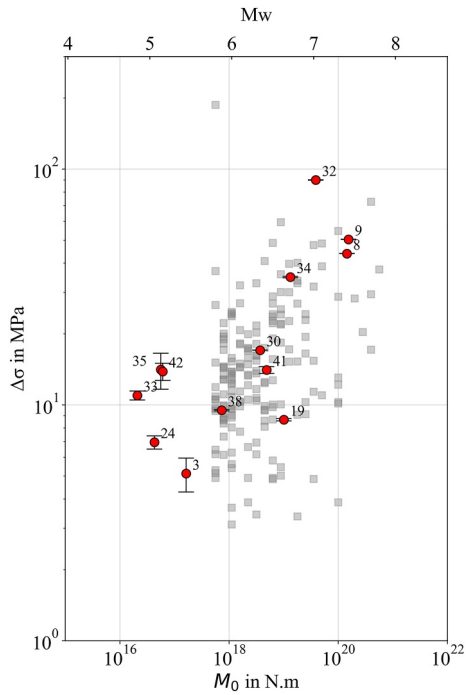

Figure 4. Average $\Delta\sigma$ for the 13 events in Table 1 plotted against the corresponding seismic moments. Solutions are numbered as in Table 1 and Table S1 in Supporting Information S1. Vertical bars represent the estimate's uncertainties. Gray squares represent estimates from Poli and Prieto (2016), comprising 180 deep-focus earthquakes ($5.8 \leq Mw \leq 7.8$) from several subduction zones between 2000 and 2016.

where ω is the angular frequency, $M(\omega)$ is the moment spectrum, c is either α (P-wave velocity) or β (S-wave velocity), and ρ is density. To assess the integral in Equation 2, the moment-rate spectrum was extrapolated to both low and high frequencies using a low-frequency average and a ω^{-1} fall-off rate, respectively, and ρ, α, and β were estimated from the AK135 velocity model (Kennett et al., 1995) according to hypocentral depth. We set the extrapolation limits for each average spectrum to the highest and lowest spectral amplitude values that were above the SNR threshold, keeping a record of the amount of energy that was extrapolated for future interpretations.

E_R estimates vary from 6.8×10^{10} J to 1.9×10^{16} J among the sequence (Table 1). In general, most E_R values represent E_R^S (Figures 5a–5c), which can range from 3 to 120 times E_R^P (Figure 5d). From Figure 5c, it is clear that E_R is roughly proportional to M_0, although we observed that some similar-sized earthquakes show quite different values of E_R. First, E_R from event 41 (6.4 Mw) is notably 9 times larger than the estimate from event 30 (6.3 Mw). Second, our estimate for event 32 (Mw 7.0), 1.9×10^{16} J, is slightly larger than our estimate for the largest ruptures in the sequence (events 8 and 9, 7.4 Mw) which showed remarkably similar E_R values of 1.06×10^{16} J and 1.23×10^{16} J, respectively. Finally, event 34 (6.7 Mw) showed much higher E_R than event 19 (6.6 Mw). Nevertheless, we note that more than 50% of the E_R for events 3, 24, 33, and 35 came from the extrapolated, high-frequency portion of the moment-rate spectra and, therefore, must be considered with care.

The scaled energy (E_R/M_0) was also examined and observed to be quite variable within the sequence (Figure 6). Clearly, event 32 showed the highest value, displaying a disproportionate release of energy from its rupture process. Events 8, 9, 34 and 41 also showed relatively high energy-to-moment ratios, while the rest of the sequence showed considerably smaller values. The scaled energy found for event 35 (5.1 Mw) is considerably higher than estimates from similar-size events (events 24 and 42). Disregarding event 33, for which a 68% of the energy was contributed by the extrapolated portion of the spectrum, event 42 displayed the smaller scaled energy. Overall, scaled energies display a suggestive but not clear trend of scaled energy increasing with magnitude (Figure 6).

4.2. Radiation Efficiency

Based on the M_0, $\Delta\sigma$, and E_R estimates for each event, we determined the radiation efficiency (η_R) as (e.g., Kanamori & Brodsky, 2004):

$$\eta_R = \frac{2\mu}{\Delta\sigma}\frac{E_R}{M_0} \tag{3}$$

in which the shear modulus (μ) was calculated based on the S-wave velocity value at the source. The η_R quantifies the proportion of energy released as elastic waves relative to the energy dissipated in the rupture process (Poli & Prieto, 2016). By definition η_R varies between 0, meaning that no energy was radiated as seismic waves, and 1, when no energy was dissipated mechanically and all energy budget, after subtracting the energy lost by friction, is transmitted as seismic waves (Kanamori & Brodsky, 2004). Values of η_R larger than 1 can sometimes be obtained, possibly reflecting either imprecise estimates of E_R and/or $\Delta\sigma$, a complex stress release process, the use of an inaccurate model to calculate η_R, or an undershoot rupture (Nishitsuji & Mori, 2014; Venkataraman & Kanamori, 2004).

We observed quite variable η_R values for the sequence under study, with values ranging from as high as 1.58 to as low as 0.07 (Figure 7). The smallest η_R value was found for event 33, which is the smallest event in the sequence, while the maximum value was observed for event 3 (5.4 Mw). These two events, however, had almost 70% of their E_R extrapolated and may not be reliable. Aside from these two extreme events, η_R values still vary

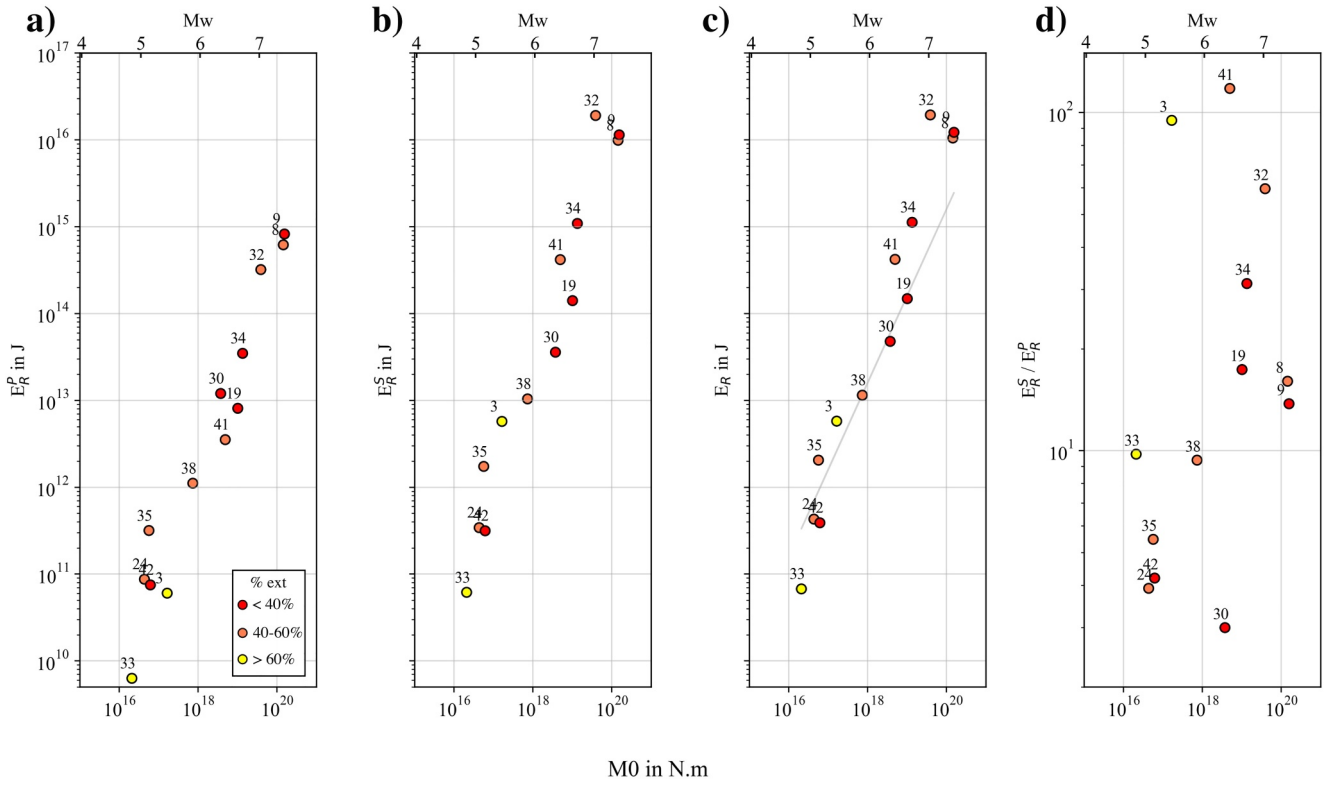

Figure 5. Estimates of E_R from the 13 events in Table 1. (a) energy radiated as P-wave, E_R^P; (b) energy radiated as S-wave, E_R^S; (c) total radiated energy, E_R; (d) ratio between E_R^S and E_R^P as a function of the seismic moment. Events are numbered as in Table 1 and color-coded by the amount of extrapolated energy in E_R. Solid gray line in c represents the $E_R = 1.6 \times 10^{-5}\ M_0$ empirical relationship from Choy and Boatwright (1995).

considerably (0.1–1.4); however, if we disregard efficiency values above 1.0, all estimates are roughly between 0.2 and 0.6. Within this reduced range, events 34 and 35 had relatively high η_R of ~0.6, while the rest of the events showed $\eta_R < 0.4$ and an average η_R of 0.3, meaning that most of the events involved relatively small η_R values (Table 1). We did not find any size dependency for η_R; in fact, similar-size events showed quite different efficiencies (see for instance events 30, 41, 19, and 34 showing η_R equal to 0.2, 1.4, 0.4, and 0.6, respectively).

5. Discussion

5.1. Variability in Stress Drop, Radiated Energy, and Seismic Efficiency

As shown in Figure 4, $\Delta\sigma$ calculated from f_c and M_0 (5–90 MPa) are all within the expected range of 1–100 MPa (e.g., Liu et al., 2020; Poli & Prieto, 2016) and hint at a mild correlation between $\Delta\sigma$ and M_0. This correlation was already observed from both intermediate-depth and deep-focus earthquakes (e.g., Liu et al., 2020; Nishitsuji & Mori, 2014; Poli & Prieto, 2016; Prieto et al., 2013). We found very high $\Delta\sigma$ for event 32 (~90 MPa) and relatively high $\Delta\sigma$ for events 8, 9 and 34 (35–50 MPa), when compared to the rest of the sequence (≤17 MPa). Also, the $\Delta\sigma$ found for events 8 and 9 are considerably higher than previous estimates (2.3–19.3 MPa) (Ruiz et al., 2017; Ye et al., 2016). Comparisons between $\Delta\sigma$ from different approaches are usually difficult to make (e.g., Abercrombie, 2021), but it is noteworthy that we determined $\Delta\sigma$ based on well-constrained f_c and M_0, which results in more reliable estimates than calculations from rupture speed (e.g., Ye et al., 2016). No depth dependency for $\Delta\sigma$ was observed, as previously noted by Liu et al. (2020) from several globally-distributed deep-focus earthquakes in the 6.0–8.2 Mw range. Note, however, that our results are now filling a significant gap at Mw ≤ 5.8 (Figure 4) and provide observations for events smaller than those in the previous global study of Poli and Prieto (2016). Also, although $\Delta\sigma$ is known to be difficult to constrain, our methodology was consistently applied for all events within the 2014–2022 sequence, which ensures the robustness of our comparisons.

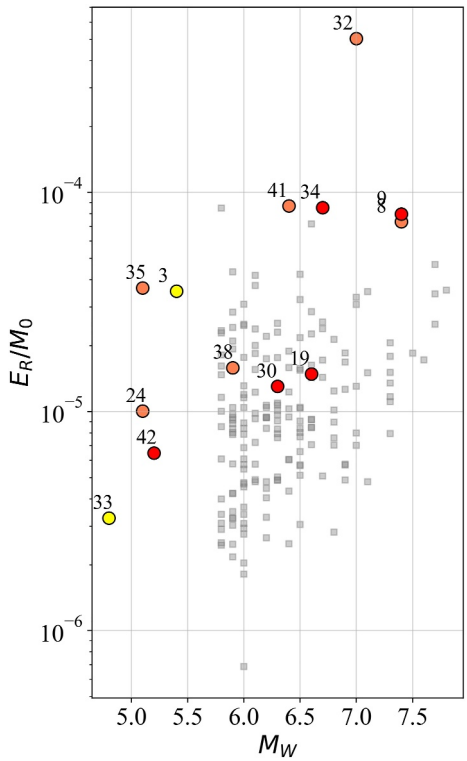

Figure 6. Scaled energy plotted as function of magnitude. Events are color-coded by the amount of extrapolation and labeled as in Table 1. Gray squares are estimates from Poli and Prieto (2016).

Globally, small-to-moderate shallow earthquakes display E_R^S values that are 9–17 times that of E_R^P (Abercrombie, 1995; Boatwright et al., 1991; Prieto et al., 2004; Viegas et al., 2010), although some events in India suggest that E_R^S can reach up to 100 times E_R^P (S. Kumar et al., 2023; V. Kumar et al., 2016, 2019). Most of our events showed $E_R^S/E_R^P < 20$, so our observations are mostly consistent with previous estimates (Figure 5d). Events 3, 32, 34 and 41 displayed large ratios ranging between 30 and 120 (Figure 5d). Disregarding event 3, which had ~70% of its E_R extrapolated, we are thus observing 3 large-size events (Mw 6.4–7.0) with anomalously high E_R^S/E_R^P ratios. Note that the most energetic event (event 32) has an E_R^S estimate that is nearly 60 times larger than the E_R^P estimate (compare Figures 5a–5c). High E_R for events 34 and 41 are also related to high E_R^S, as inferred from their E_R^S/E_R^P ratios of 31 and 118, respectively. The ratio of 118 is notably higher than observed in previous studies.

To confirm that events 32, 34 and 41 are anomalously energetic, we compared their seismograms with similar-size earthquakes at select stations. We were careful to select nearby stations away from nodal planes. It is worth noting that focal mechanisms from the Peru-Brazil segment usually show a consistent normal faulting pattern (Leite Neto et al., 2024a). For the Mw 7.0 event 32, we compared its waveforms with those from the Mw 6.7 event 34 (Figure 8). We observe that, for frequencies above 0.05 Hz, the S-wave amplitude content relative to the P-wave amplitude content is larger for event 32 than for event 34. This observation explains the disproportionate E_R^S/E_R^P value for event 32 and why it was anomalously energetic (Figures 5c and 5d). We also compared its waveforms with those from the Mw 7.4 event 8 (Figure S7 in Supporting Information S1), with similar conclusions. Other comparisons (event 34 with the Mw 6.6 events 19, and event 41 with Mw 6.3 event 30) further confirmed this anomalous S-wave energy release at higher frequencies (Figures S5–S8 in Supporting Information S1). It is tempting to infer that events with magnitude above 6.4 Mw tend to release more energy compared to smaller ones.

We observe that, in general, our E_R estimates tend to increase with M_0, as predicted by the empirical relationship derived from globally distributed shallow earthquakes of Choy and Boatwright (1995) (Figure 5c). However, events 8, 9, 32, 33, 34, and 41 are at odds with this observation, although event 33 had almost 70% of its energy estimate extrapolated. Overall, scaled energies are all below 10^{-4}, in agreement with independent compilations (e.g., Kanamori & Brodsky, 2004), and suggest that they are proportional to earthquake magnitude, although it is less apparent if we disregard the two extreme values (events 33 and 32). However, as demonstrated above, event 32 was indeed very energetic and yields a robust observation for an anomalously high scaled energy. In any case, the scaling (or lack thereof) between E_R and M_0 remains inconclusive due to large uncertainties in E_R, with some authors advocating for it (Abercrombie, 1995; Mayeda & Walter, 1996) and others arguing against it (Choy & Boatwright, 1995; Ide & Beroza, 2001; Ide et al., 2003; Prieto et al., 2004). If the scaling were real, it would imply that larger ruptures are more efficient in releasing energy as seismic waves (Prieto et al., 2004).

The variation in source parameters reported in the previous sections results in a notable variability in seismic efficiency within the deep-focus sequence under study. We found that most of the sequence showed $\eta_R < 0.4$, but some discrepant values were observed. Discrepant events included: (a) Mw 6.4 event 41 and Mw 7.0 event 32 with $\eta_R \geq 1.3$; and (b) Mw 5.1 event 35 and Mw 6.7 event 34 with $\eta_R \sim 0.6$. We also found no size dependency. The very high η_R obtained for events 41 and 32 resulted from their high scaled energies (Figure 6), produced by the disproportionate release of E_R during their ruptures (Figure 5). It is noteworthy that event 32 also involved the highest $\Delta\sigma$ within the sequence, and thus E_R for this event was remarkably high and yielded an also high $\eta_R = 1.3$. The relatively high η_R found for event 34 can also be explained through its high scaled energy (Figure 6). Realize that, in spite of events 34 and 41 having similar scaled energies, η_R for event 34 is smaller because of its higher $\Delta\sigma$ of 34.8 MPa. Similarly, a high η_R for event 35 is also related to a high E_R, especially when compared to events with similar sizes and $\Delta\sigma$ (events 24 and 42). Events 42 and 30 presented the lowest η_R among our deep-focus

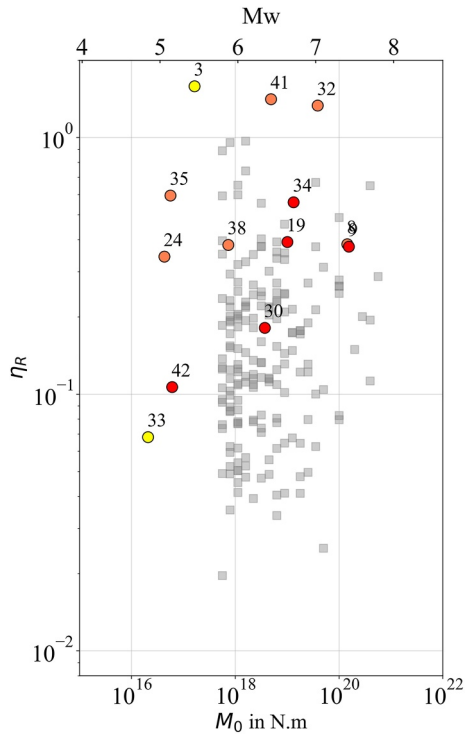

Figure 7. Radiation efficiency plotted as function of the seismic moment. Events are color-coded by the amount of extrapolation and labeled as in Table 1. Gray squares are estimates calculated based on the apparent stresses and stress drops of Poli and Prieto (2016).

events, resulting from their relatively low scaled energies compared to the rest of the sequence (Figure 6). The η_R estimated for the 2015 doublet agree with previous estimates (Ruiz et al., 2017).

5.2. Assessing the Robustness of Our Findings Considering Different Q Assumptions

Estimates of f_c, and consequently of $\Delta\sigma$, are known to be dependent on correctly accounting for attenuation when modeling the spectra, as it can be equally described with either a small f_c and large Q, or a large f_c and small Q (e.g., Abercrombie, 2021; Ko et al., 2012; Nakai et al., 2021; Scherbaum, 1990; Tian et al., 2022). This trade-off constitutes a major source of uncertainty when determining f_c, which are even larger when calculating the $\Delta\sigma$ (Equation 1) (e.g., Abercrombie, 2015, 2021; Chang et al., 2023; Shearer et al., 2019). In fact, whether observed variations in $\Delta\sigma$ reflect a fundamental inter-event difference or result from measurement uncertainties remains a topic of considerable debate (e.g., Baltay et al., 2024). It is worth noting that the ongoing Community Stress Drop Validation Study is conducting a systematic comparison between $\Delta\sigma$ estimated from different approaches using the same 2019 Ridgecrest sequence data set aiming at better understanding this variability (Baltay et al., 2024). Similarly, since most of the E_R is released at frequencies greater than f_c, this parameter is also dependent on attenuation, as the shorter periods are more sensitive to the detailed attenuation structure (Abercrombie, 1995, 2021; Baltay et al., 2024). This fact contributes to making scaled energy estimates as uncertain as $\Delta\sigma$ estimates (Abercrombie, 2021). Logically, as η_R is determined from $\Delta\sigma$ and E_R (Equation 3), it is inevitably affected by these uncertainties.

Considering this trade-off between path and source, we explored how our findings vary with different Q assumptions by conducting three tests. First, we repeated the study with the same assumption of $Q_P = Q_S$ but using other values of Q (500, 700, 1,000, 1,500, and 2,000) (Figure S25 in Supporting Information S1). Second, we repeated the study for different combinations of Q_P and Q_S, considering $Q_P > Q_S$ (Figures S27–S29 in Supporting Information S1). Third, we again assumed $Q_P = Q_S$ but now considering the spatial variations in Q expected for a subduction zone setting (e.g., Tian et al., 2022) (see the two groups of stations in Figure S30 in Supporting Information S1 and the results in Figures S31–S33 in Supporting Information S1).

In all three tests, we observed that in general the absolute values of $\Delta\sigma$ tend to decrease as Q increases, a direct consequence of the aforementioned trade-off (see Figures S25, S27, and S31 in Supporting Information S1). From the first test, which assumes $Q_P = Q_S$, we found that Q must be greater than 500 in order to resolve f_c, as our results with $Q = 500$ results in the saturation of f_c at the maximum allowed value of 50 Hz and consequently in very high and linearly distributed $\Delta\sigma$ (Figure S25 in Supporting Information S1). From $Q = 700$ to $Q = 2{,}000$, we observed that the scaling with M_0 becomes more evident, especially from $Q = 1{,}000$ to $Q = 2000$. Similarly, scaled energies were also observed to decrease in absolute value with increasing Q and to exhibit a more pronounced scaling with event size as Q increases (Figures S25, S28, and S32 in Supporting Information S1). Q values of less than 700 seem insufficient to account for attenuation in our spectra as it leads to both an increase in the amount of extrapolation in E_R, which is observed even for the largest events within our sequence, and a considerable departure from the empirical relationship of Choy and Boatwright (1995) (Figure S26 in Supporting Information S1). Such small Q values also result in scaled energy estimates that are mostly above the expected limit of 10^{-4}, further suggesting that Q must be larger (Figure S25 in Supporting Information S1). Scaling in both $\Delta\sigma$ and scaled energy was observed for most of the combinations between Q_P and Q_S, when $Q_S \geq 800$, or between Q_1 and Q_2, when $Q_2 \geq 800$ (see Figures S27 and S31 in Supporting Information S1), therefore suggesting that scaling is robust, and that Q must be greater than ~800 to model our data. In the investigated range of Q, which reaches up to 2000, we did not see an upper limit of Q for modeling our data, as little difference was observed in our estimates from $Q = 1{,}500$ to $Q = 2{,}000$ (Figure S25 in Supporting Information S1). However, as $\Delta\sigma$ continue to decrease, we suppose that further increasing Q may eventually lead to underestimating this parameter.

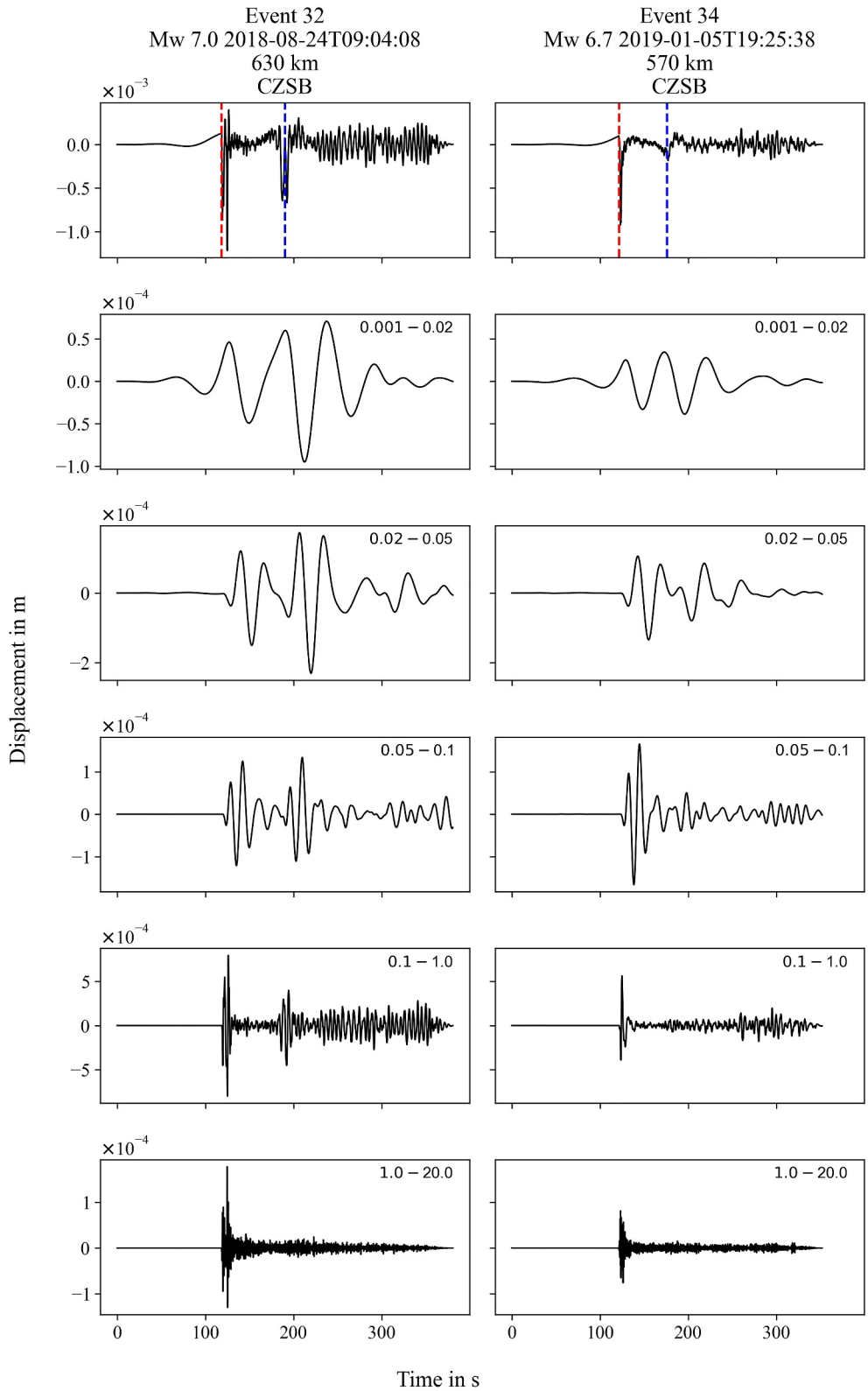

Figure 8. Comparison between vertical seismograms for event 32 and event 34 at station CZSB at different frequency ranges. P- and S-wave arrivals are shown as dashed red and blue lines on the broadband seismograms (upper panels). The frequency ranges used for filtering are shown in the upper right corner of each panel.

In terms of η_R, its variability within the sequence was found to be consistent among all our examinations (Figures S25, S29, and S33 in Supporting Information S1). Considering $Q_P = Q_S$, we observed that Q greater than or equal to 1,000 results in more reasonable η_R estimates (Figure S25 in Supporting Information S1). Perhaps more interestingly, when using a $Q > 1{,}000$ all η_R estimates become smaller than 1, as expected from Equation 3. Now considering $Q_P \neq Q_S$, we observed that Q_S must be at least of 1,000 in order to produce reasonable η_R estimates, but we were only able to put all estimates almost below 1 when $Q_S \geq 1{,}200$ (Figure S29 in Supporting Information S1). Allowing spatial variations in Q, we observed reasonable estimates of η_R for all combinations with $Q_2 \geq 800$, and that all estimates are smaller than 1 when $Q_2 \geq 1{,}000$ (Figure S33 in Supporting Information S1). From these results, we might conclude that underestimating Q be responsible for the $\eta_R > 1$ found for events 32 and 41. On the other hand, if we assume that E_R and $\Delta\sigma$ are well determined for these events, $\eta_R > 1$ could imply that they resulted from undershoot ruptures (e.g., Venkataraman & Kanamori, 2004). Undershoot occurs when the final static stress is higher than the final dynamic stress, leading to a decrease in $\Delta\sigma$ accompanied by an increase in E_R (Abercrombie, 2021; Poli & Prieto, 2016; Venkataraman & Kanamori, 2004). Yet another possibility that deserves investigation is that these anomalous η_R are resulting from insufficient azimuthal coverage. In this sense, if the inversion for f_c relies on stations concentrated along a particular azimuth, consequently sampling a particular rupture direction, estimates of f_c can be biased. However, we found no significant difference in the azimuthal coverage for the two anomalous events compared to the rest of the sequence, as shown in Figure S24 in Supporting Information S1. Concluding, regardless on the feasibility of our $\eta_R > 1$ estimates, the variability in η_R within the sequence is robust.

5.3. Nucleation of Deep-Focus Earthquakes Along the Peru-Brazil Segment

Large deep-focus events (Mw > 7) in South America (Nazca), and in other warm subducting plates such as Japan, are usually the product of very dissipative ruptures characterized by very low efficiencies ($\eta_R < 0.1$) (Estabrook, 1999; Tibi et al., 2003; Venkataraman & Kanamori, 2004). For instance, because the 1994 Mw 8.2 Bolivia earthquake was characterized by a very low η_R of ∼0.04, high $\Delta\sigma$ of 110–283 MPa and slow rupture velocity of 1–2 km/s, it is widely accepted that melting assisted such large slip over a relatively small area (40×40 km^2) (Goes & Ritsema, 1995; Ihmlé, 1998; Kanamori et al., 1998; Kikuchi & Kanamori, 1994; Zhan et al., 2014). The 1970 Mw 8.1 Colombia earthquake and the 1963 Mw 7.7 Peru-Bolivia earthquake also displayed very low $\eta_R \sim 0.01$ and low rupture speeds (2 km/s), but low-to-moderate $\Delta\sigma$ of 39.4 and 18 MPa, respectively (Estabrook, 1999). The 1991 Mw 7.2 Argentina earthquake, on the other hand, displayed a cold slab-like behavior. The high $\eta_R = 0.3$, high rupture speed of 3.5 km/s and low $\Delta\sigma$ of 5 MPa reported for this event were interpreted as due to little melting during its rupture, possibly related to its nucleation in a relatively colder section of the Nazca slab (Tibi et al., 2003). For comparison, some large deep-focus earthquakes (Mw 7.0–7.9) in cold slabs (e.g., Fiji-Tonga, Bonin and Mariana) showed η_R ranging from 0.1 to 0.6 (e.g., Tibi et al., 2003).

Similar to the Argentina earthquake, we observed η_R in the 0.34–0.39 range for several events in the Peru-Brazil sequence under study (events 8, 9, 19, 24 and 38, 5.1–7.4 Mw). In addition, previous studies pointed to relatively large rupture speeds, between 2.25 and 3.2 km/s, for events 8 and 9 (e.g., Ruiz et al., 2017). More efficient ruptures ($\eta_R \sim 0.6$) were also observed within the Peru-Brazil sequence for event 34 (6.7 Mw) and event 35 (5.1 Mw), even events with $\eta_R > 1$ (event 32, 7.0 Mw; event 41, 6.4 Mw) that suggested two very efficient or brittle-like ruptures. Events 30 (6.3 Mw) and 42 (5.2 Mw), on the other hand, presented the lowest efficiencies ($\eta_R \leq 0.18$) within the sequence, but still higher than estimates found in Colombia and Bolivia.

The Nazca plate is often regarded as a warm plate because its thermal parameter is under 2,500 km (Frohlich, 2006). Note that this parameter is obtained from plate age and subduction speed, which characterize the subducting plate at shallow depths and do not necessarily reflect its thermal structure at large depths. Indeed, most of our η_R seem consistent with a relatively cold segment of the Nazca plate as they contrast with those reported for other (warmer) segments (e.g., Colombia and Bolivia). One possibility is that this segment of the Nazca plate be thermally composite, with a warm upper half consistent with the observed thermal parameter, and a cold lower-half consistent with large efficiencies. Interestingly, a composite thermal structure has been proposed due to either an abrupt change in the age of the subducting lithosphere (Engebretson & Kirby, 1992; Kirby et al., 1995; Okal & Bina, 1994) or to a reduction in subduction speed caused by the subduction of the Nazca ridge (Leite Neto et al., 2024a). Both hypotheses propose the transition would occur at around 500 km depth and explain the nucleation of deep-focus events within a narrow 500–700 km depth range through a thin MOW preserved in the

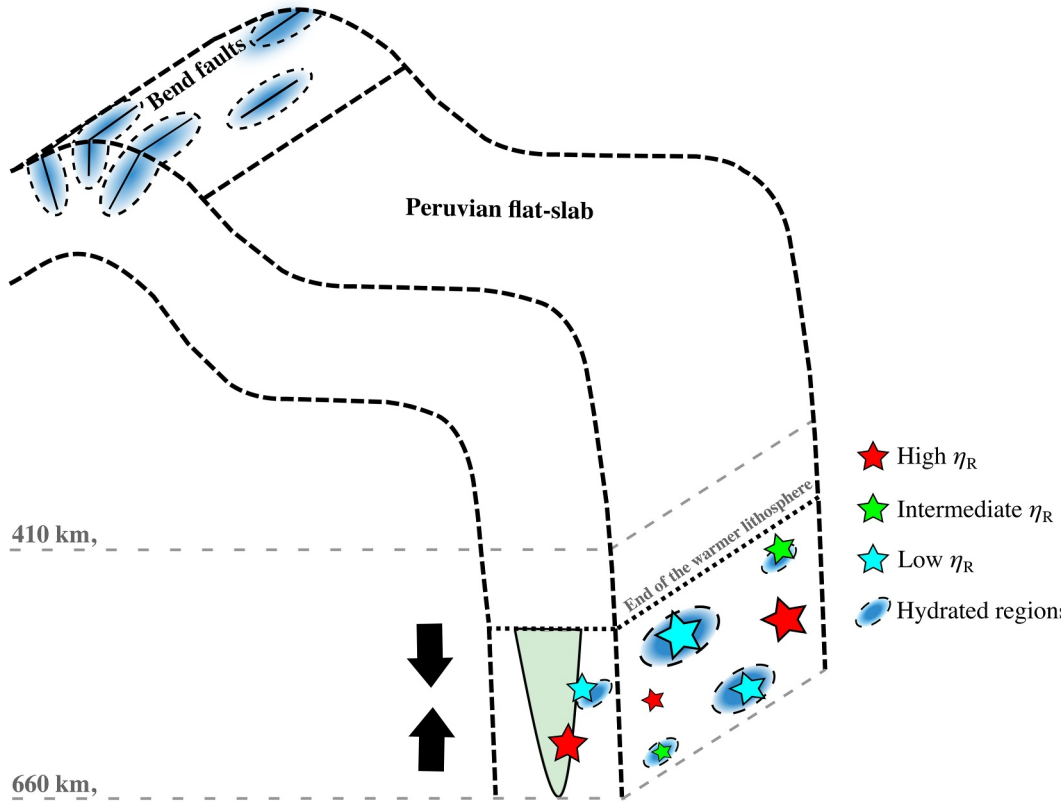

Figure 9. Schematic model proposed to explain variable η_R for deep-focus earthquakes in the Peru-Brazil segment. Outer rise faults promote localized deep hydration of mantle rocks that can survive down to mantle transition zone depths in the form of small-scale slab heterogeneities. Deep-focus events are explained as the result of transformational faulting and thermal runaway controlled by the dehydration reactions in such hydrated regions near the source. Transformational faulting in a preserved metastable olivine wedge could explain the confinement of deep-focus seismicity to a narrow depth range (~500–700 km). The more or less dissipative behavior of the rupture is thus explained by the amount of melting involved in the thermal runaway step, which is possibly controlled by the amount of fluids released by the dehydration reactions when available. Figure S34 in Supporting Information S1 illustrates the spatial variability of η_R and $\Delta\sigma$ within the studied slab segment.

interior of the cold lower half of the slab. If this were correct, ruptures could be being nucleated through transformational faulting within a thin MOW and propagated beyond its limits via thermal runaway (Zhan, 2017).

Counterintuitively, however, we found no relationship between η_R and M_0 suggestive of event size being related to increased viscosity reduction or melting in the fault zone. Furthermore, we found no clear spatial pattern in η_R that would indicate any regional patterns within the slab (Figure S9 in Supporting Information S1). The two $\eta_R \sim 0.6$ happened at the north end of the sequence, but the two $\eta_R > 1$ happened at distant locations separated by events with $\eta_R < 0.4$. It is thus possible that very local physical conditions within the source region be controlling the dissipative (lower η_R) or brittle-like (higher η_R) character of the ruptures. We thus propose that the character of the rupture depends on small-scale heterogeneities within the source region (Figure 9). Such heterogeneities could be related to localized hydrated mantle rocks formed by deep hydration at outer rise faults (e.g., Fujie et al., 2018; Kita & Ferrand, 2018; Mao et al., 2022; Ranero et al., 2003). In this model, the observed brittle-like ruptures would occur in specific regions of the slab where little or no dehydration is expected to occur, thus involving little or no melting during its propagation via thermal runaway. Regions where considerable amounts of water can be released by dehydration, on the other hand, could explain less efficient ruptures through increased amounts of melt.

Moreover, note that dehydration reactions could assist transformational faulting through either water precipitation around the grains and/or through the release of elevated stresses that would be transmitted to the MOW (Ferrand, 2019; Ferrand et al., 2017; Mao et al., 2022). Conversely, transformational faulting itself could promote

dehydration reactions through the release of latent heat or through temperature increase near the fault zone by shear heating. The water and heat released from these processes would allow for more or less melting in the fault zone, which would depend on the amount of fluids that can be released. This interplay between heat released by transformational faulting and water released by dehydration reactions would ultimately be responsible for the short-scale variations in seismic efficiency.

As a final note, because water enhances olivine phase transformations (e.g., Du Frane et al., 2013; Hosoya et al., 2005; Kubo et al., 1998), it has been assumed that the presence of a MOW must necessarily be linked to a dry oceanic lithosphere, suggesting the simultaneous occurrence of dehydration and transformational faulting is incompatible (Du Frane et al., 2013; Kawakatsu & Yoshioka, 2011; Shen & Zhan, 2020; Zhan, 2020). However, there has been evidence that hydrous phase A in the subducting lithosphere may act as a sponge in the MTZ up to ~1000°C, thus avoiding saturation of olivine and wadsleyite and preserving the MOW (Ishii & Ohtani, 2021). The eventual dehydration of hydrous phase A under high enough temperatures would favor the fast exothermic reactions required for transformational faulting to occur. In this case, water could play a role in the nucleation of anticracks and in allowing for more melting in the fault zone. Water as a catalyst of deep-focus earthquakes was already proposed by Mao et al. (2022) to explain higher b-values found in regions of Japan where the lithospheric mantle of the Pacific plate is expected to be highly hydrated. Also, sublithospheric diamonds originated from the MTZ are strong evidence that water is being released at depths where such events occur (Pearson et al., 2014; Shirey et al., 2021; Wiens, 2021).

6. Conclusions

We determined seismic source parameters (M_0, f_c, $\Delta\sigma$, E_R, and η_R) for a total of 13 deep-focus events ($4.8 \leq \text{Mw} \leq 7.4$) between 2014 and 2022 in the Peru-Brazil segment. The obtained f_c (0.13–3.7 Hz) tend to decrease with M_0, but not as predicted by self-similarity, resulting in notable variations in $\Delta\sigma$ (5.1–89.8 MPa). E_R estimates are within the 6.8×10^{10}–1.9×10^{16} J range and are generally proportional to M_0, although some large events (Mw > 6.4) displayed a disproportional release of E_R. η_R presented remarkable variability within the sequence, ranging from 0.1 to 1.4. Particularly, two events showed $\eta_R > 1$, implying in very efficient ruptures, while other two events presented $\eta_R \leq 0.18$, evidencing more dissipative events. Given the relatively small source area we argue that, at the very least, our relative efficiency estimates are robust, meaning that the large variability of seismic efficiency is a real feature. We thus propose that earthquakes are able to occur in this region due to the presence of a MOW preserved within a cold slab segment attached to the warm Nazca plate at MTZ depths. Faulting would then initiate by transformational faulting and then further propagate by thermal runaway. During the propagation stage, more or less melting in the fault zone could explain variable η_R, and the amount of melting would depend on the presence of small-scale hydrated regions near the source. These hypothesized heterogeneities could be possibly linked to deep hydration promoted by bend faults at the outer rise.

Data Availability Statement

All data used in this work are made available as a Zenodo data set (https://doi.org/10.5281/zenodo.10685298) (Leite Neto et al., 2024b). This data set comprises stations from different networks distributed over the South American continent, which are summarized in Table S2 in Supporting Information S1. In Brazil, we used data from the University of Brasilia Seismic Network (BR), the Rede Sismográfica do Nordeste do Brasil (NB), both belonging to the Brazilian Seismic Network (RSBR), and data from the temporary 3-Basin Project (XC) (Assumpção & Bianchi, 2016), which also includes a station in Bolívia. Data from both RSBR and XC are open and can be obtained through the FDSNWS server (http://seisrequest.iag.usp.br/fdsnws/dataselect/1/) from the USP Seismological Center (USPSC). In Chile, we used data from three networks: the Red Sismológica Nacional (C1) (Universidad de Chile, 2012), the Chilean National Seismic Network (C), and the Plate Boundary Observatory Network Northern Chile/IPOC seismic network (CX) (GFZ German Research Centre for Geosciences; Institut des Sciences De l'Univers-Centre National de la Recherche CNRS-INSU, 2006). We also used stations from the Red Sismológica Nacional de Colombia (CM) (Servicio Geológico Colombiano, 1993) and the Ecuador Seismic Network (EC). Data from international networks were also included: GEOFON (GE) (GEOFON Data Centre, 1993), and GSN (II and IU) (Scripps Institution of Oceanography, 1986; Albuquerque Seismological Laboratory/USGS, 2014). Data from C1, C, CX, CM, EC, GE, II, and IU can be requested through the EarthScope Consortium Wilber 3 system (https://ds.iris.edu/wilber3/).

Acknowledgments
We express our gratitude to the Editor handling our manuscript, Rachel Abercrombie, and the Associate Editor, as well as to Piero Poli and an anonymous reviewer for their insightful comments, which greatly enhanced the quality of this paper. GSLN expresses gratitude to the Coordenação de Aperfeiçoamento de Pessoal de Nível Superior (CAPES) for his PhD scholarship and for his exchange scholarship (Programa de Doutorado Sanduíche no Exterior - PDSE/CAPES)—Finance Code 001. JJ is grateful to the Conselho Nacional de Desenvolvimento Científico e Tecnológico (CNPq) for their support, provided through a research grant (award n. 434807/2018-4) and a continuing research fellowship (award n. 310261/2023-6). Finally, we thank Marcelo Assumpção and the Instituto de Astronomia, Geofísica e Ciências Atmosféricas of the Universidade de São Paulo (IAG/USP) for providing access to data from the 3-Basin Project network (XC).

References

Abercrombie, R. E. (1995). Earthquake source scaling relationships from −1 to 5 ML using seismograms recorded at 2.5-km depth. *Journal of Geophysical Research*, *100*(B12), 24015–24036. https://doi.org/10.1029/95JB02397

Abercrombie, R. E. (2015). Investigating uncertainties in empirical Green's function analysis of earthquake source parameters. *Journal of Geophysical Research: Solid Earth*, *120*(6), 4263–4277. https://doi.org/10.1002/2015JB011984

Abercrombie, R. E. (2021). Resolution and uncertainties in estimates of earthquake stress drop and energy release. *Philosophical Transactions of the Royal Society A*, *379*(2196), 20200131. https://doi.org/10.1098/rsta.2020.0131

Abercrombie, R. E., Bannister, S., Ristau, J., & Doser, D. (2017). Variability of earthquake stress drop in a subduction setting, the Hikurangi Margin, New Zealand. *Geophysical Journal International*, *208*(1), 306–320. https://doi.org/10.1093/gji/ggw393

Albuquerque Seismological Laboratory/USGS. (2014). Global Seismograph Network (GSN - IRIS/USGS) [Dataset]. *International Federation of Digital Seismograph Networks*. https://doi.org/10.7914/SN/IU

Assumpção, M. S., & Bianchi, M. B. (2016). Pantanal, Chaco and Paraná (PCPB) structural studies network [Dataset]. *USP Seismological Center (USPSC)*. https://doi.org/10.7914/8scf-yd39

Baltay, A., Abercrombie, R. E., Chu, S., & Taira, T. (2024). The SCEC/USGS community stress drop validation study using the 2019 Ridgecrest earthquake sequence. *Seismica*, *3*(1). https://doi.org/10.26443/seismica.v3i1.1009

Baltay, A., Prieto, G. A., & Beroza, G. C. (2010). Radiated seismic energy from coda measurements and no scaling in apparent stress with seismic moment. *Journal of Geophysical Research*, *115*(B8), B08314. https://doi.org/10.1029/2009JB006736

Bianchi, M. B., Assumpção, M., Rocha, M. P., Carvalho, J. M., Azevedo, P. A., Fontes, S. L., et al. (2018). The Brazilian seismographic network (RSBR): Improving seismic monitoring in Brazil. *Seismological Research Letters*, *89*(2A), 452–457. https://doi.org/10.1785/0220170227

Boatwright, J., & Fletcher, J. B. (1984). The partition of radiated energy between P and S waves. *Bulletin of the Seismological Society of America*, *74*(2), 361–376. https://doi.org/10.1785/BSSA0740020361

Boatwright, J., Fletcher, J. B., & Fumal, T. E. (1991). A general inversion scheme for source, site, and propagation characteristics using multiply recorded sets of moderate-sized earthquakes. *Bulletin of the Seismological Society of America*, *81*(5), 1754–1782. https://doi.org/10.1785/BSSA0810051754

Booth, C. M., Forsyth, D. W., & Weeraratne, D. S. (2014). Upper mantle *Q* structure beneath old seafloor in the western Pacific. *Journal of Geophysical Research: Solid Earth*, *119*(4), 3448–3461. https://doi.org/10.1002/2013JB010589

Bos, A. G., Nolet, G., Rubin, A., Houston, H., & Vidale, J. E. (1998). Duration of deep earthquakes determined by stacking of Global Seismograph Network seismograms. *Journal of Geophysical Research*, *103*(B9), 21059–21065. https://doi.org/10.1029/98JB01352

Brune, J. N. (1970). Tectonic stress and the spectra of seismic shear waves from earthquakes. *Journal of Geophysical Research*, *75*(26), 4997–5009. https://doi.org/10.1029/JB075i026p04997

Campus, P., & Das, S. (2000). Comparison of the rupture and radiation characteristics of intermediate and deep earthquakes. *Journal of Geophysical Research*, *105*(B3), 6177–6189. https://doi.org/10.1029/1999JB900384

Chang, H., Abercrombie, R. E., Nakata, N., Pennington, C. N., Kemna, K. B., Cochran, E. S., & Harrington, R. M. (2023). Quantifying site effects and their influence on earthquake source parameter estimations using a dense array in Oklahoma. *Journal of Geophysical Research: Solid Earth*, *128*(9), e2023JB027144. https://doi.org/10.1029/2023JB027144

Choy, G. L., & Boatwright, J. L. (1995). Global patterns of radiated seismic energy and apparent stress. *Journal of Geophysical Research*, *100*(B9), 18205–18228. https://doi.org/10.1029/95JB01969

Crotwell, H. P., Owens, T. J., & Ritsema, G. (1999). The TauP Toolkit: Flexible seismic travel-time and ray-path utilities. *Seismological Research Letters*, *70*(2), 154–160. https://doi.org/10.1785/gssrl.70.2.154

Devaux, J. P., Schubert, G., & Anderson, C. (1997). Formation of a metastable olivine wedge in a descending slab. *Journal of Geophysical Research*, *102*(B11), 24627–24637. https://doi.org/10.1029/97JB02334

Du Frane, W. L., Sharp, T. G., Mosenfelder, J. L., & Leinenweber, K. (2013). Ringwoodite growth rates from olivine with ~75 ppmw H_2O: Metastable olivine must be nearly anhydrous to exist in the mantle transition zone. *Physics of the Earth and Planetary Interiors*, *219*, 1–10. https://doi.org/10.1016/j.pepi.2013.04.001

Eberhart-Phillips, D., Reyners, M., Chadwick, M., & Stuart, G. (2008). Three-dimensional attenuation structure of the Hikurangi subduction zone in the central North Island, New Zealand. *Geophysical Journal International*, *174*(1), 418–434. https://doi.org/10.1111/j.1365-246X.2008.03816.x

Efron, B., & Tibshirani, R. (1991). Statistical data analysis in the computer age. *Science*, *253*(5018), 390–395. https://doi.org/10.1126/science.253.5018.390

Engebretson, D. C., & Kirby, S. H. (1992). Deep Nazca slab seismicity: Why is it so anomalous? *Eos, Transactions, American Geophysical Union*, *73*(43), 379. [abstract].

Eshelby, J. D. (1957). The determination of the elastic field of an ellipsoidal inclusion, and related problems. *Proceedings of the Royal Society of London. Series A. Mathematical and Physical Sciences*, *241*(1226), 376–396. https://doi.org/10.1098/rspa.1957.0133

Estabrook, C. H. (1999). Body wave inversion of the 1970 and 1963 South American large deep-focus earthquakes. *Journal of Geophysical Research*, *104*(B12), 28751–28767. https://doi.org/10.1029/1999JB900244

Ferrand, T. P. (2019). Seismicity and mineral destabilizations in the subducting mantle up to 6 GPa, 200 km depth. *Lithos*, *334–335*, 205–230. https://doi.org/10.1016/j.lithos.2019.03.014

Ferrand, T. P., Hilairet, N., Incel, S., Deldicque, D., Labrousse, L., Gasc, J., et al. (2017). Dehydration-driven stress transfer triggers intermediate-depth earthquakes. *Nature Communications*, *8*(1), 15247. https://doi.org/10.1038/ncomms15247

Frohlich, C. (1989). The nature of deep-focus earthquakes. *Annual Review of Earth and Planetary Sciences*, *17*(1), 227–254. https://doi.org/10.1146/annurev.earth.17.1.227

Frohlich, C. (2006). *Deep earthquakes*. Cambridge University Press. https://doi.org/10.1017/CBO9781107297562

Fujie, G., Kodaira, S., Kaiho, Y., Yamamoto, Y., Takahashi, T., Miura, S., & Yamada, T. (2018). Controlling factor of incoming plate hydration at the north-western Pacific margin. *Nature Communications*, *9*(3844), 3844. https://doi.org/10.1038/s41467-018-06320-z

Furumura, T., Kennett, B. L. N., & Padhy, S. (2016). Enhanced waveguide effect for deep-focus earthquakes in the subducting Pacific slab produced by a metastable olivine wedge. *Journal of Geophysical Research: Solid Earth*, *121*(9), 6779–6796. https://doi.org/10.1002/2016JB013300

GEOFON Data Centre. (1993). GEOFON Seismic Network [Dataset]. *Deutsches GeoForschungsZentrum GFZ*. https://doi.org/10.14470/TR560404

GFZ German Research Centre for Geosciences; Institut des Sciences De l'Univers-Centre National de la Recherche CNRS-INSU. (2006). IPOC Seismic Network [Dataset]. *Integrated Plate boundary Observatory Chile – IPOC*. https://doi.org/10.14470/PK615318

Goes, S., & Ritsema, J. (1995). A broadband P wave analysis of the large deep Fiji Island and Bolivia Earthquakes of 1994. *Geophysical Research Letters*, *22*(16), 2249–2252. https://doi.org/10.1029/95GL02011

Green, H. W., & Burnley, P. C. (1989). A new self-organizing mechanism for deep-focus earthquakes. *Nature*, *341*(6244), 733–737. https://doi.org/10.1038/341733a0

Green, H. W., & Marone, C. (2002). Instability of deformation. *Reviews in Mineralogy and Geochemistry*, *51*(1), 181–199. https://doi.org/10.2138/gsrmg.51.1.181

Green, H. W., & Zhou, Y. (1996). Transformation-induced faulting requires an exothermic reaction and explains the cessation of earthquakes at the base of the mantle transition zone. *Tectonophysics*, *256*(1–4), 39–56. https://doi.org/10.1016/0040-1951(95)00164-6

Havskov, J., & Ottemoller, L. (2010). Routine data processing in earthquake seismology. https://doi.org/10.1007/978-90-481-8697-6

Hosoya, T., Kubo, T., Ohtani, E., Sano, A., & Funakoshi, K. (2005). Water controls the fields of metastable olivine in cold subducting slabs. *Geophysical Research Letters*, *32*(17), L17305. https://doi.org/10.1029/2005GL023398

Houston, H. (2015). Deep earthquakes. In *Treatise on Geophysics* (pp. 329–354). Elsevier. https://doi.org/10.1016/B978-0-444-53802-4.00079-8

Houston, H., Benz, H. M., & Vidale, J. E. (1998). Time functions of deep earthquakes from broadband and short-period stacks. *Journal of Geophysical Research*, *103*(B12), 29895–29913. https://doi.org/10.1029/98JB02135

Ide, S., & Beroza, G. C. (2001). Does apparent stress vary with earthquake size? *Geophysical Research Letters*, *28*(17), 3349–3352. https://doi.org/10.1029/2001GL013106

Ide, S., Beroza, G. C., Prejean, S. G., & Ellsworth, W. L. (2003). Apparent break in earthquake scaling due to path and site effects on deep borehole recordings. *Journal of Geophysical Research*, *108*(B5), 2271. https://doi.org/10.1029/2001JB001617

Ihmlé, P. F. (1998). On the interpretation of subevents in teleseismic waveforms: The 1994 Bolivia deep earthquake revisited. *Journal of Geophysical Research*, *103*(B8), 17919–17932. https://doi.org/10.1029/98JB00603

Ishii, T., & Ohtani, E. (2021). Dry metastable olivine and slab deformation in a wet subducting slab. *Nature Geoscience*, *14*(7), 526–530. https://doi.org/10.1038/s41561-021-00756-7

Jiang, G., & Zhao, D. (2011). Metastable olivine wedge in the subducting Pacific slab and its relation to deep earthquakes. *Journal of Asian Earth Sciences*, *42*(6), 1411–1423. https://doi.org/10.1016/j.jseaes.2011.08.005

Jiménez, C., Calvo, C., Saavedra, M., Moggiano, N., & Molina, W. (2021). Source characteristics of Peruvian deep focus seismic doublet of November 24, 2015. *Journal of South American Earth Sciences*, *105*, 102919. https://doi.org/10.1016/j.jsames.2020.102919

Kanamori, H., Anderson, D. L., & Heaton, T. H. (1998). Frictional melting during the rupture of the 1994 Bolivian earthquake. *Science*, *279*(5352), 839–842. https://doi.org/10.1126/science.279.5352.839

Kanamori, H., & Brodsky, E. E. (2004). The physics of earthquakes. *Reports on Progress in Physics*, *67*(8), 1429–1496. https://doi.org/10.1088/0034-4885/67/8/R03

Kaneko, Y., & Shearer, P. M. (2014). Seismic source spectra and estimated stress drop derived from cohesive-zone models of circular subshear rupture. *Geophysical Journal International*, *197*(2), 1002–1015. https://doi.org/10.1093/gji/ggu030

Kawakatsu, H., & Yoshioka, S. (2011). Metastable olivine wedge and deep dry cold slab beneath southwest Japan. *Earth and Planetary Science Letters*, *303*(1–2), 1–10. https://doi.org/10.1016/j.epsl.2011.01.008

Kennett, B. L. N., Engdahl, E. R., & Buland, R. (1995). Constraints on seismic velocities in the Earth from traveltimes. *Geophysical Journal International*, *122*(1), 108–124. https://doi.org/10.1111/j.1365-246X.1995.tb03540.x

Kikuchi, M., & Kanamori, H. (1994). The mechanism of the Deep Bolivia Earthquake of June 9, 1994. *Geophysical Research Letters*, *21*(22), 2341–2344. https://doi.org/10.1029/94GL02483

Kirby, S. H., Durham, W. B., & Stern, L. A. (1991). Mantle phase changes and deep-earthquake faulting in subducting lithosphere. *Science*, *252*(5003), 216–225. https://doi.org/10.1126/science.252.5003.216

Kirby, S. H., Okal, E. A., & Engdahl, E. R. (1995). The 9 June 94 Bolivian Deep Earthquake: An exceptional event in an extraordinary subduction zone. *Geophysical Research Letters*, *22*(16), 2233–2236. https://doi.org/10.1029/95GL01802

Kirby, S. H., Stein, S., Okal, E. A., & Rubie, D. C. (1996). Metastable mantle phase transformations and deep earthquakes in subducting oceanic lithosphere. *Reviews of Geophysics*, *34*(2), 261–306. https://doi.org/10.1029/96RG01050

Kita, S., & Ferrand, T. P. (2018). Physical mechanisms of oceanic mantle earthquakes: Comparison of natural and experimental events. *Scientific Reports*, *8*(1), 17049. https://doi.org/10.1038/s41598-018-35290-x

Ko, Y., Kuo, B., & Hung, S. (2012). Robust determination of earthquake source parameters and mantle attenuation. *Journal of Geophysical Research*, *117*(B4), B04304. https://doi.org/10.1029/2011JB008759

Kubo, T., Ohtani, E., Kato, T., Shinmei, T., & Fujino, K. (1998). Effects of water on the α-β transformation kinetics in San Carlos olivine. *Science*, *281*(5373), 85–87. https://doi.org/10.1126/science.281.5373.85

Kumar, S., Kumar, D., Singh, A. P., & Rastogi, B. K. (2023). Source parameters and scaling relations for small earthquakes in the Saurashtra Horst of Western Deccan Volcanic Province, India and its seismotectonic implications. *Journal of Earth System Science*, *132*(3), 118. https://doi.org/10.1007/s12040-023-02130-0

Kumar, V., Kumar, D., & Chopra, S. (2016). Estimation of source parameters and scaling relations for moderate size earthquakes in North-West Himalaya. *Journal of Asian Earth Sciences*, *128*, 79–89. https://doi.org/10.1016/j.jseaes.2016.07.023

Kumar, V., Kumar, D., & Chopra, S. (2019). Source parameters and scaling relations for moderate size earthquakes in north–east India region. *Pure and Applied Geophysics*, *176*(1), 45–64. https://doi.org/10.1007/s00024-018-1972-0

Lay, T., & Wallace, T. (1995). *Modern global seismology*. Elsevier.

Leite Neto, G. S., Julià, J., & Prieto, G. A. (2024a). Deep-focus earthquake mechanisms at the subducting Nazca plate (Peru-Brazil border): Cold slab behavior in a warm plate. *Earth and Space Science*, *11*(10), e2024EA003617. https://doi.org/10.1029/2024EA003617

Leite Neto, G. S., Julià, J., & Prieto, G. A. (2024b). Seismograms for deep-focus earthquakes in the Peru-Brazil region [Dataset]. *Zenodo*. https://doi.org/10.5281/ZENODO.10685297

Liu, M., Huang, Y., & Ritsema, J. (2020). Stress drop variation of deep-focus earthquakes based on empirical Green's functions. *Geophysical Research Letters*, *47*(9), e2019GL086055. https://doi.org/10.1029/2019GL086055

Madariaga, R. (1976). Dynamics of an expanding circular fault. *Bulletin of the Seismological Society of America*, *66*(3), 639–666. https://doi.org/10.1785/BSSA0660030639

Mao, G. L., Ferrand, T. P., Li, J., Zhu, B., Xi, Z., & Chen, M. (2022). Unsupervised machine learning reveals slab hydration variations from deep earthquake distributions beneath the northwest Pacific. *Communications Earth & Environment*, *3*(1), 56. https://doi.org/10.1038/s43247-022-00377-x

Mayeda, K., & Walter, W. R. (1996). Moment, energy, stress drop, and source spectra of western United States earthquakes from regional coda envelopes. *Journal of Geophysical Research*, *101*(B5), 11195–11208. https://doi.org/10.1029/96JB00112

Mosenfelder, J. L., Marton, F. C., Ross, C. R., Kerschhofer, L., & Rubie, D. C. (2001). Experimental constraints on the depth of olivine metastability in subducting lithosphere. *Physics of the Earth and Planetary Interiors*, *127*(1–4), 165–180. https://doi.org/10.1016/S0031-9201(01)00226-6

Nakai, J. S., Sheehan, A. F., Abercrombie, R. E., & Eberhart-Phillips, D. (2021). Near trench 3D seismic attenuation offshore Northern Hikurangi subduction margin, North Island, New Zealand. *Journal of Geophysical Research: Solid Earth*, *126*(3), e2020JB020810. https://doi.org/10.1029/2020JB020810

Nishitsuji, Y., & Mori, J. (2014). Source parameters and radiation efficiency for intermediate-depth earthquakes in Northeast Japan. *Geophysical Journal International*, *196*(2), 1247–1259. https://doi.org/10.1093/gji/ggt458

Ohuchi, T., Higo, Y., Tange, Y., Sakai, T., Matsuda, K., & Irifune, T. (2022). In situ X-ray and acoustic observations of deep seismic faulting upon phase transitions in olivine. *Nature Communications*, *13*(1), 5213. https://doi.org/10.1038/s41467-022-32923-8

Okal, E. A., & Bina, C. R. (1994). The deep earthquakes of 1921–1922 in Northern Peru. *Physics of the Earth and Planetary Interiors*, *87*(1–2), 33–54. https://doi.org/10.1016/0031-9201(94)90020-5

Pearson, D. G., Brenker, F. E., Nestola, F., McNeill, J., Nasdala, L., Hutchison, M. T., et al. (2014). Hydrous mantle transition zone indicated by ringwoodite included within diamond. *Nature*, *507*(7491), 221–224. https://doi.org/10.1038/nature13080

Persh, S. E., & Houston, H. (2004). Deep earthquake rupture histories determined by global stacking of broadband P waveforms. *Journal of Geophysical Research*, *109*(B4), B04311. https://doi.org/10.1029/2003JB002762

Poli, P., & Prieto, G. (2014). Global and along-strike variations of source duration and scaling for intermediate-depth and deep-focus earthquakes. *Geophysical Research Letters*, *41*(23), 8315–8324. https://doi.org/10.1002/2014GL061916

Poli, P., & Prieto, G. A. (2016). Global rupture parameters for deep and intermediate-depth earthquakes. *Journal of Geophysical Research: Solid Earth*, *121*(12), 8871–8887. https://doi.org/10.1002/2016JB013521

Prieto, G. A. (2022). The multitaper spectrum analysis package in Python. *Seismological Research Letters*, *93*(3), 1922–1929. https://doi.org/10.1785/0220210332

Prieto, G. A., Florez, M., Barrett, S. A., Beroza, G. C., Pedraza, P., Blanco, J. F., & Poveda, E. (2013). Seismic evidence for thermal runaway during intermediate-depth earthquake rupture. *Geophysical Research Letters*, *40*(23), 6064–6068. https://doi.org/10.1002/2013GL058109

Prieto, G. A., Shearer, P. M., Vernon, F. L., & Kilb, D. (2004). Earthquake source scaling and self-similarity estimation from stacking P and S spectra. *Journal of Geophysical Research*, *109*(B8), B08310. https://doi.org/10.1029/2004JB003084

Prieto, G. A., Thomson, D. J., Vernon, F. L., Shearer, P. M., & Parker, R. L. (2007). Confidence intervals for earthquake source parameters. *Geophysical Journal International*, *168*(3), 1227–1234. https://doi.org/10.1111/j.1365-246X.2006.03257.x

Raleigh, C. B. (1967). Tectonic implications of serpentinite weakening. *Geophysical Journal International*, *14*(1–4), 113–118. https://doi.org/10.1111/j.1365-246X.1967.tb06229.x

Ranero, C. R., Phipps Morgan, J., McIntosh, K., & Reichert, C. (2003). Bending-related faulting and mantle serpentinization at the Middle America trench. *Nature*, *425*(6956), 367–373. https://doi.org/10.1038/nature01961

Ruiz, S., Tavera, H., Poli, P., Herrera, C., Flores, C., Rivera, E., & Madariaga, R. (2017). The deep Peru 2015 doublet earthquakes. *Earth and Planetary Science Letters*, *478*, 102–109. https://doi.org/10.1016/j.epsl.2017.08.036

Scherbaum, F. (1990). Combined inversion for the three-dimensional *Q* structure and source parameters using microearthquake spectra. *Journal of Geophysical Research*, *95*(B8), 12423–12438. https://doi.org/10.1029/JB095iB08p12423

Scripps Institution of Oceanography. (1986). Global Seismographic Network – IRIS/IDA [Dataset]. *International Federation of Digital Seismograph Networks*. https://doi.org/10.7914/SN/II

Servicio Geológico Colombiano. (1993). Red Sismologica Nacional de Colombia [Dataset]. *International Federation of Digital Seismograph Networks*. https://doi.org/10.7914/SN/CM

Shearer, P. M., Abercrombie, R. E., Trugman, D. T., & Wang, W. (2019). Comparing EGF methods for estimating corner frequency and stress drop from P wave spectra. *Journal of Geophysical Research: Solid Earth*, *124*(4), 3966–3986. https://doi.org/10.1029/2018JB016957

Shen, Z., & Zhan, Z. (2020). Metastable olivine wedge beneath the Japan sea imaged by seismic interferometry. *Geophysical Research Letters*, *47*(6), e2019GL085665. https://doi.org/10.1029/2019GL085665

Shirey, S. B., Wagner, L. S., Walter, M. J., Pearson, D. G., & van Keken, P. E. (2021). Slab transport of fluids to deep focus earthquake depths—Thermal modeling constraints and evidence from diamonds. *AGU Advances*, *2*(2), e2020AV000304. https://doi.org/10.1029/2020AV000304

Thomson, D. J. (1982). Spectrum estimation and harmonic analysis. *Proceedings of the IEEE*, *70*(9), 1055–1096. https://doi.org/10.1109/PROC.1982.12433

Tian, D., Wei, S. S., Wang, W., & Wang, F. (2022). Stress drops of intermediate-depth and deep earthquakes in the Tonga slab. *Journal of Geophysical Research: Solid Earth*, *127*(10), e2022JB025109. https://doi.org/10.1029/2022JB025109

Tibi, R., Bock, G., & Wiens, D. A. (2003). Source characteristics of large deep earthquakes: Constraint on the faulting mechanism at great depths. *Journal of Geophysical Research*, *108*(B2), 2091. https://doi.org/10.1029/2002JB001948

Tocheport, A., Rivera, L., & Chevrot, S. (2007). A systematic study of source time functions and moment tensors of intermediate and deep earthquakes. *Journal of Geophysical Research*, *112*(B7), B07311. https://doi.org/10.1029/2006JB004534

Tsallis, C. (1988). Possible generalization of Boltzmann-Gibbs statistics. *Journal of Statistical Physics*, *52*(1–2), 479–487. https://doi.org/10.1007/BF01016429

Tsallis, C., & Stariolo, D. A. (1996). Generalized simulated annealing. *Physica A: Statistical Mechanics and Its Applications*, *233*(1–2), 395–406. https://doi.org/10.1016/S0378-4371(96)00271-3

Universidad de Chile. (2012). Red Sismologica Nacional [Dataset]. *International Federation of Digital Seismograph Networks*. https://doi.org/10.7914/SN/C1

Venkataraman, A., & Kanamori, H. (2004). Observational constraints on the fracture energy of subduction zone earthquakes. *Journal of Geophysical Research*, *109*(B5), B05302. https://doi.org/10.1029/2003JB002549

Viegas, G., Abercrombie, R. E., & Kim, W.-Y. (2010). The 2002 M5 Au Sable Forks, NY, earthquake sequence: Source scaling relationships and energy budget. *Journal of Geophysical Research*, *115*(B7), B07310. https://doi.org/10.1029/2009JB006799

Wiens, D. A. (2021). Diamonds hold clues about the cause of deep earthquakes. *AGU Advances*, *2*(2), e2021AV000434. https://doi.org/10.1029/2021AV000434

Xiang, Y., Sun, D. Y., Fan, W., & Gong, X. G. (1997). Generalized simulated annealing algorithm and its application to the Thomson model. *Physics Letters A*, *233*(3), 216–220. https://doi.org/10.1016/S0375-9601(97)00474-X

Ye, L., Lay, T., Kanamori, H., Zhan, Z., & Duputel, Z. (2016). Diverse rupture processes in the 2015 Peru deep earthquake doublet. *Science Advances*, *2*(6), e1600581. https://doi.org/10.1126/sciadv.1600581

Zahradník, J., Čížková, H., Bina, C. R., Sokos, E., Janský, J., Tavera, H., & Carvalho, J. (2017). A recent deep earthquake doublet in light of long-term evolution of Nazca subduction. *Scientific Reports*, *7*(1), 45153. https://doi.org/10.1038/srep45153

Zhan, Z. (2017). Gutenberg–Richter law for deep earthquakes revisited: A dual-mechanism hypothesis. *Earth and Planetary Science Letters*, *461*, 1–7. https://doi.org/10.1016/j.epsl.2016.12.030

Zhan, Z. (2020). Mechanisms and implications of deep earthquakes. *Annual Review of Earth and Planetary Sciences*, *48*(1), 147–174. https://doi.org/10.1146/annurev-earth-053018-060314

Zhan, Z., Kanamori, H., Tsai, V. C., Helmberger, D. V., & Wei, S. (2014). Rupture complexity of the 1994 Bolivia and 2013 Sea of Okhotsk deep earthquakes. *Earth and Planetary Science Letters*, *385*, 89–96. https://doi.org/10.1016/j.epsl.2013.10.028

References From the Supporting Information

Hayes, G. P., Moore, G. L., Portner, D. E., Hearne, M., Flamme, H., Furtney, M., & Smoczyk, G. M. (2018). Slab2, a comprehensive subduction zone geometry model. *Science*, *362*(6410), 58–61. https://doi.org/10.1126/science.aat4723